Tandem metalloenzymes gate plant cell entry by pathogenic fungi

Bastien Bissaro, Sayo Kodama, Takumi Nishiuchi, Anna Maria Díaz-Rovira, Hayat Hage, David Ribeaucourt, Mireille Haon, Sacha Grisel, A. Jalila Simaan, Fred Beisson, et al.

Tandem metalloenzymes gate plant cell entry by pathogenic fungi

Bastien Bissaro[1†], Sayo Kodama[2†], Takumi Nishiuchi[3], Anna Maria Díaz-Rovira[4], Hayat Hage[1], David Ribeaucourt[1,6,7], Mireille Haon[1], Sacha Grisel[1], A. Jalila Simaan[6], Fred Beisson[8], Stephanie M. Forget[9], Harry Brumer[9], Marie-Noëlle Rosso[1], Victor Guallar[4,5], Richard O´Connell[10], Mickaël Lafond[6], Yasuyuki Kubo[2*] and Jean-Guy Berrin[1*]

[1]INRAE, Aix Marseille Université, UMR1163 Biodiversité et Biotechnologie Fongiques, 13009, Marseille, France
[2]Faculty of Agriculture, Setsunan University, 573-0101, Osaka, Japan
[3]Division of Functional Genomics, Advanced Science Research Center, Kanazawa University, 920-0934 Kanazawa, Japan
[4]Barcelona Supercomputing Center, Plaça Eusebi Güell, 1-3, E-08034 Barcelona, Spain
[5]ICREA, Passeig Lluís Companys 23, E-08010 Barcelona, Spain
[6]Aix Marseille Université, CNRS, Centrale Marseille, iSm2, Marseille, France
[7] V. Mane Fils, 620 route de Grasse, 06620 Le Bar sur Loup, France
[8]CEA, CNRS, Aix Marseille Université, Institut de Biosciences et Biotechnologies d'Aix-Marseille (UMR7265), CEA Cadarache, 13108 Saint-Paul-lez-Durance, France
[9] Michael Smith Laboratories, University of British Columbia, 2185 East Mall, Vancouver, BC, V6T 1Z4, Canada
[10] INRAE, UMR BIOGER, AgroParisTech, Université Paris-Saclay, Thiverval-Grignon, France

*Correspondence to: Yasuyuki Kubo (yasuyuki.kubo@setsunan.ac.jp) and Jean-Guy Berrin (jean-guy.berrin@inrae.fr)

†These authors contributed equally

Abstract

Global food security is endangered by fungal phytopathogens causing devastating crop production losses. Many of these pathogens use specialized appressoria cells to puncture plant cuticles. Here, we unveil a pair of alcohol oxidase-peroxidase enzymes to be essential for pathogenicity. Using *Colletotrichum orbiculare*, we show that the enzyme pair is co-secreted by the fungus early during plant penetration, and that single and double mutants have impaired penetration ability. Molecular modeling, biochemical and biophysical approaches revealed a fine-tuned interplay between these metalloenzymes, which oxidize plant cuticular long-chain alcohols into aldehydes. We show that the enzyme pair is involved in transcriptional regulation of genes necessary for host penetration. The identification of these infection-specific metalloenzymes opens new avenues on the role of wax-derived compounds and the design of oxidase-specific inhibitors for crop protection.

Short title:
Fungal metalloenzymes drive plant invasion.

One Sentence Summary:
Fungal phytopathogens secrete tandem metalloenzymes that catalyze cuticle oxidation and drive plant cell entry.

Introduction

Fungal phytopathogens represent a serious threat to plant health (*1*) and global food security (*2*). *Colletotrichum* and *Magnaporthe* species rank among the top 10 most devastating fungal phytopathogens in the world and reduce crop yield by up to 30% (*3*). Despite being separated by ca. 300 million years of evolution (*4, 5*), these fungi share remarkable similarities in their infection strategy, notably the formation of a specialized cell dedicated to host penetration called an appressorium (*6–8*) (**Fig. 1A**). This dome-shaped, darkly melanized cell generates a high internal turgor and directs this mechanical pressure onto a needle-like penetration peg (*9–11*), which emerges from a 2-500 nm pore at the appressorial base to puncture the plant's outer defensive barriers, namely the cuticle and epidermal cell wall. Despite major advances in our understanding of the cellular processes preceding (*6, 7, 11–14*) and following (*15, 16*) plant cell entry, the (bio)chemical reactions occurring at this nanoscale plant-fungus interface and their role in host penetration are not fully elucidated.

Copper radical oxidases (CROs) are enzymes with diverse substrate specificities, and have been extensively studied since the late 1960s (*17*). Today, CROs include galactose 6-oxidases (GalOx) (*17*), glyoxal oxidases (*18*), and broad specificity primary alcohol oxidases (AlcOx) (*19, 20*). Despite the detailed knowledge available on the enzymology and structure of CROs, their biological function remains largely unknown. It has only been proposed that glyoxal oxidases play a role in lignin degradation by fungal saprotrophs (*18*). During the course of our previous work (*19*), we noted that genes encoding secreted AlcOx orthologs are particularly widespread among phytopathogenic ascomycete fungi and are absent in plants. Given that long-chain primary alcohols are components of the waxy cuticle of aerial plant surfaces (*21*), we hypothesized that AlcOx could play a role in fungal pathogenesis.

In this study, we used a combination of 'omics analyses to unveil the pairing of AlcOx with a redox partner, namely heme-peroxidase, in some fungal plant pathogens of high agricultural importance. We used wet enzymology and molecular modeling to demonstrate and characterize the interplay between these metalloenzymes. Reverse genetics, live-cell imaging and fungal transcriptomics allowed us to probe the *in vivo* function of the enzyme pair, providing new molecular insights into the host penetration cascade.

Results

Discovery of the tandem Perox-AlcOx

While studying the enzymology of *Colletotrichum* AlcOx enzymes for biotechnological applications (*19, 22*), we noticed the presence of a gene encoding a putative peroxidase located adjacent to an AlcOx-encoding gene (**Fig. 1B**). To strengthen this initial observation, we searched for *alcox* orthologs in 30 sequenced *Colletotrichum* genomes, which revealed the near-ubiquitous presence of a putative peroxidase (hereafter called "Tandem Peroxidase"). Interestingly, the *perox* and *alcox* genes were found in a head-to-head arrangement (**fig. S1**), suggesting the presence of a bidirectional promoter for tight co-expression of the genes. Interestingly, these Tandem Peroxidases are never found in combination with other types of CROs (**fig. S1C**) and both proteins encoded by the *perox-alcox* pair are predicted to be secreted (**Table S1**). These observations aroused our interest because

it is known that CROs require activation by horseradish peroxidase (HRP) for maximum activity *in vitro* (*23*, *24*).

Our phylogenetic analysis of the peroxidase-catalase superfamily showed that the Tandem Peroxidases cluster together in a sister clade within the under-explored ascomycete Class II peroxidases (*25*) (**fig. S2A**). Furthermore, Tandem Peroxidases form a distinct clade amongst the 333 Class II peroxidases found in *Colletotrichum* species (**fig. S2B**), suggestive of neofunctionalization. A broad search for the co-occurrence of *perox* and *alcox* orthologs across fungal genomes revealed that the pair is also present in *Magnaporthe* species, including the infamous causal agent of rice blast, *Magnaporthe oryzae* (syn. *Pyricularia oryzae*) (**Table S2**). Mapping the occurrence of Perox-AlcOx protein pairs and their corresponding genomic neighborhoods onto a phylogeny of representative pathogenic ascomycetes (**Fig. 1B**, **fig. S3**) allowed us to conclude that the pair is present in most *Colletotrichum* species complexes for which genome sequences are available and in *Magnaporthe spp.*, and that the head-to-head organization of the pair is conserved in all these fungi, suggesting there is selection pressure to retain the pairing and that it is has a critical role in the biology of these pathogens (**Fig. 1B**).

To further test the hypothesis of a functional linkage of the *perox* and *alcox* gene products, we parsed transcriptomic data available for those fungal species harboring the pair. Remarkably, this analysis revealed that both genes are always tightly co-transcribed at the appressorium stage in various pathosystems involving *Colletotrichum* species attacking maize, fruits, and model plants (*26*, *27*), and in *M. oryzae* attacking rice and barley (*28*, *29*) (**Fig. 1C and D**). In each case, the transcript levels are relatively low and detected within a narrow time window, which may explain why these genes were overlooked in previous studies.
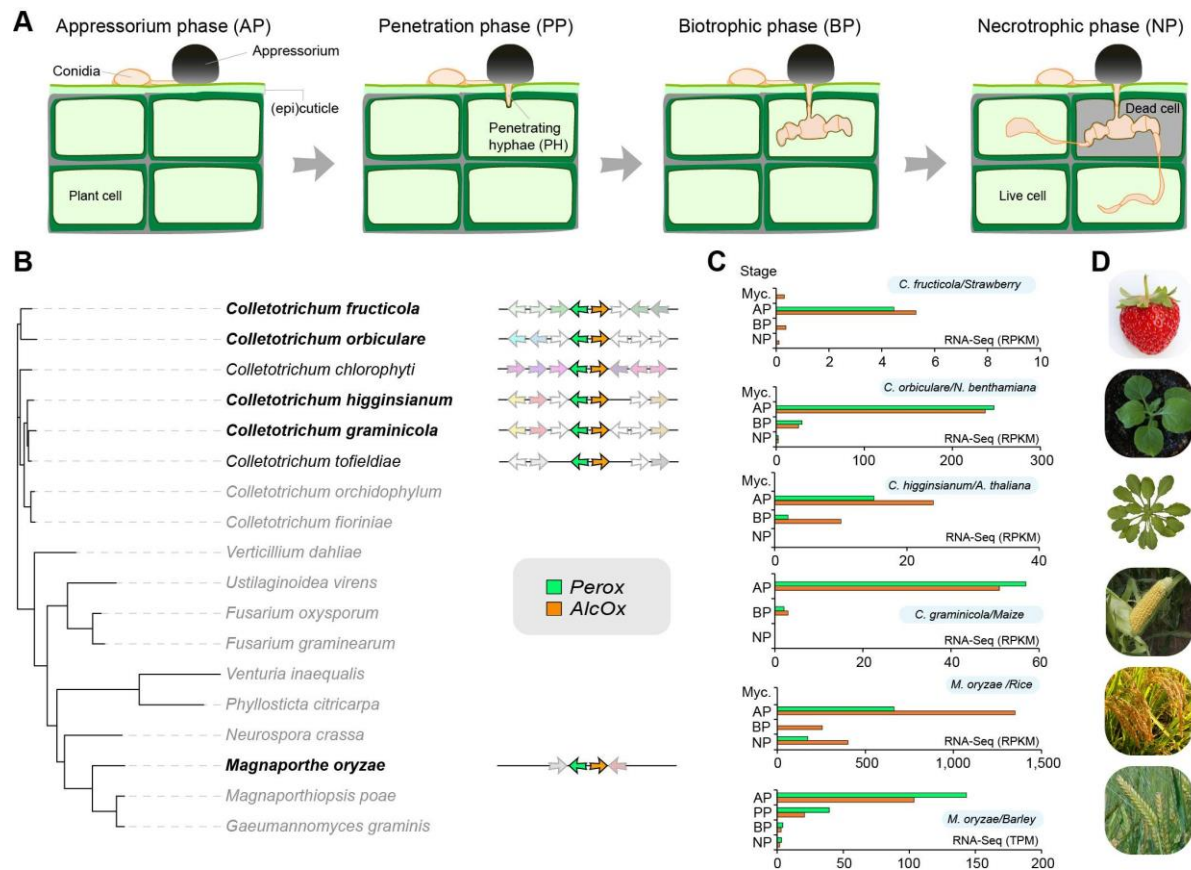
109
110 **Fig. 1. Genomic and transcriptomic analysis of the Perox-AlcOx pair. (A)** The multistage plant
111 infection process of appressorium-forming fungi: appressorium (AP), penetration (PP), biotrophic (BP)
112 and necrotrophic (NP) phases. **(B)** Phylogenomic occurrence of the *perox-alcox* pair and consensus
113 genomic environment (within each clade) amongst pathogenic ascomycetes (black bold lettering
114 indicates species for which transcriptomics data are shown in panel C, and grey lettering indicates
115 absence of the gene pair. Note that analogous tandem oxidases systems may occur in other fungi but
116 were possibly not detected due to the stringent sequence identity thresholds used to define AlcOx and
117 Perox-encoding genes. Selected *Colletotrichum* species and associated consensus sequences are
118 representative of their respective species complexes; see **fig. S3**). **(C)** Time-course transcriptomic
119 analysis of the Tandem Peroxidases (Perox, green) and AlcOx (orange) encoding genes (gene accession
120 numbers in **Table S1**) during plant infection for different pathosystems (Myc., Mycelium) (*26–29*).
121 Actual time points associated with each infection stages are provided in the Material and Methods
122 section. **(D)** Illustration of targeted plant hosts.

4

Tandem Perox-AlcOx oxidize plant long chain alcohols

As a prelude to analyzing their biological function *in vivo*, we studied the substrate specificity and enzyme interplay of the Perox-AlcOx pair *in vitro* (**Fig. 2A**). *C. orbiculare* was selected as a model because it not only causes the economically important anthracnose disease of cucurbits (e.g., melons, cucumber) but also has been used for decades as a model system for studying fungal pathogenesis (*30*). Despite the notorious difficulties associated with heterologous expression of such metalloenzymes, we successfully produced in the yeast *Pichia pastoris* recombinant copper-radical AlcOx and heme-iron tandem peroxidase from *C. orbiculare* (hereafter *Cor*AlcOx and *Cor*Perox, respectively). Similar to the previously studied AlcOx orthologs from *C. graminicola* and *C. gloeosporioides* (*19*) (**fig. S1A**), *Cor*AlcOx oxidized both aromatic and long-chain aliphatic primary alcohols (**fig. S4A**). This finding raises the possibility that fatty primary alcohols present in the cuticle of many plant species (*21*), including cucumber, could be the native substrates of these enzymes.

On the other hand, *Cor*Perox was confirmed to be a peroxidase, albeit with moderate catalytic efficiency ($k_{cat} = 1.52 \pm 0.02$ s^{-1}, $K_M^{H2O2} = 80 \pm 3$ µM, $k_{cat}/K_M = 1.9 \times 10^4 \pm 0.1$ s^{-1} M^{-1}) compared to the only previously characterized ascomycete Class II peroxidase (*25*), commercial horseradish peroxidase (HRP) (*31*), and well-studied basidiomycete lignin-active peroxidases (*32*) ($k_{cat}/K_M = 10^4$-10^7 s^{-1} M^{-1}). *Cor*Perox was only active on low redox-potential substrates and not on any of the substrates of canonical lignin-active peroxidases (**fig. S4B**), and required the presence of calcium ions for stability (**fig. S4C**). These observations are in agreement with structural predictions (**fig. S5**), which indicate the presence of two conserved calcium ion binding sites, but absence of the manganese binding site and the surface-exposed tryptophan involved in long-range electron transfer, which are two key features of lignin-active peroxidases (*33*).

Despite its comparatively low peroxidase activity, *Cor*Perox activates *Cor*AlcOx for oxidation of primary alcohols in a dose-dependent manner, and to a much greater extent than the plant peroxidase HRP does (**Fig. 2B**). The pH optima of *Cor*AlcOx and *Cor*Perox were markedly different (ca. 8 and 4, respectively, **fig. S4D**). Importantly, the pH of the environment measured on cucumber cotyledons at the time of triggering appressorium penetration by *C. orbiculare* was between 7.5 and 8.0. Taken together, these results indicate that AlcOx activation is not dependent on highly efficient peroxidase activity. We also heterologously produced the Perox-AlcOx pair from the rice blast pathogen *M. oryzae*, of which *Mor*AlcOx was recently confirmed to be a primary alcohol oxidase (*34*). Here, we obtained an activation profile for the *Mor*Perox-*Mor*AlcOx pair resembling that observed for the *C. orbiculare* pair (**fig. S4E** *cf.* **Fig. 2B**).

Having determined optimal enzyme activation conditions, we then probed further the activity of the *Cor*Perox-*Cor*AlcOx pair on biologically relevant aliphatic alcohols. Despite challenges associated with substrate solubility in aqueous buffer, we clearly detected activity on hexadecan-1,16-diol and octadecan-1-ol, as well as on a crude preparation of waxes extracted from cucumber cotyledons (**Fig. 2C**). Importantly, such activity was detected only when both enzymes were present. Product analysis by gas chromatography unambiguously indicated that octadecan-1-ol was oxidized to the corresponding aldehyde (**fig. S4F**).

To obtain a deeper understanding of the activation of AlcOx by the Tandem Peroxidase, we analyzed electron transfer by electron paramagnetic resonance (EPR) spectroscopy (**Fig.**

2D) and state-of-the art molecular modeling (**Fig. 2E and fig. S6**). Reduction in the EPR signal of the *inactive* Cu(II)-non-radical form of *Cor*AlcOx upon addition of *Cor*Perox was supportive of one-electron oxidation leading to the EPR silent, *active* Cu(II)-radical form (**Fig. 2A and D**). This change in electronic structure, observed in the absence of any substrate, confirms the activity-independent activating role of *Cor*Perox. It also indicates a close contact between the enzymes during the activation process, which is concordant with our modeling studies (see below) and with the sigmoidal, titration-like curves observed during activity assays carried out in the presence of substrate (**Fig. 2B**). Further, *Cor*AlcOx-*Cor*Perox top 5 models predicted by two independent computational techniques, PIPER (*35*) and AlphaFold2-Multimer (*36*) consistently placed *Cor*Perox structures in front of the *Cor*AlcOx active site (**fig. S6A**). Refinement of these models with the all atom Monte Carlo software PELE (*37*), which includes protein small rotations and translations followed by an exhaustive side-chain prediction at the interface, resulted in a clear minimum (**fig. S6B**) where the heme group of *Cor*Perox is oriented towards the *Cor*AlcOx copper ion (**Fig. 2E and fig. S6C**). Notably, the binding surfaces of AlcOx orthologs are considerably more hydrophobic than that of GalOx (**fig. S7A and B**), which is consistent with the idea that AlcOx may have evolved to interact with the hydrophobic plant cuticle. Moreover, in the top model (**Fig. 2E**), there is a significant decrease of solvent exposure of the *Cor*AlcOx active site, defining a cavity between both enzymes that could facilitate diffusion and binding of a long-chain alcohol substrate. C18 docking and PELE induced fit simulations confirm this point, revealing a pronounced local minimum in which the alcoholic group of the substrate is well-positioned for catalysis (**fig. S6D**).
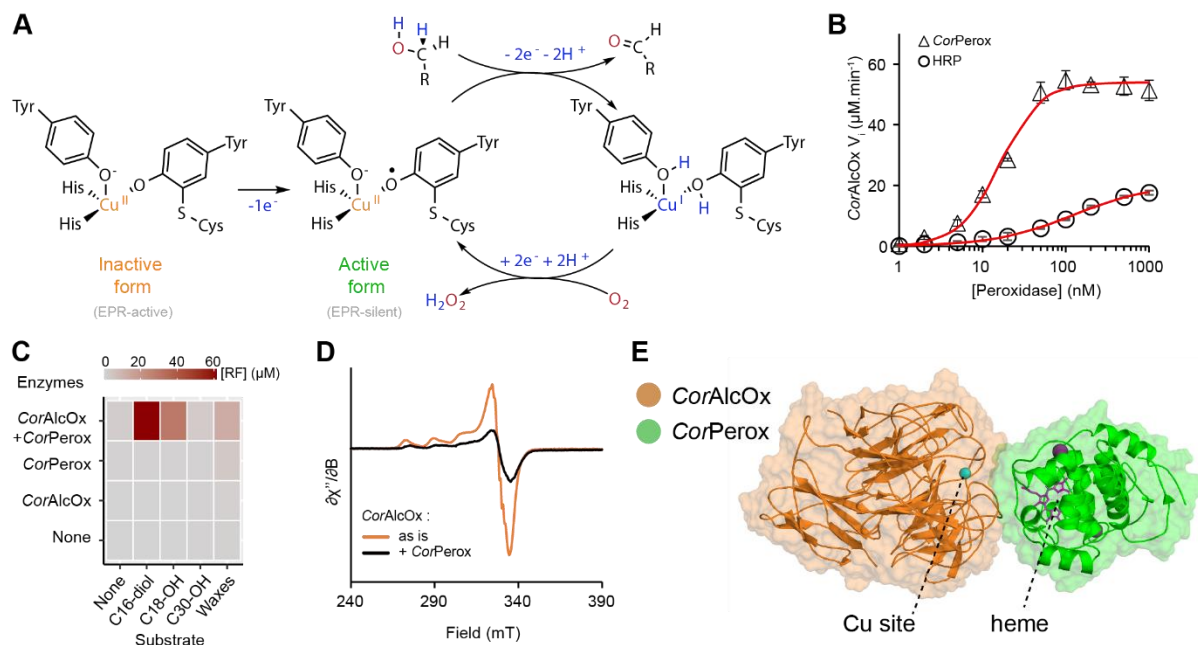
189

190
191
192 **Fig. 2. Biochemical and biophysical evidence for interplay between *Cor*Perox and *Cor*AlcOx. (A)**
193 Reaction mechanism of CROs showing activation of the resting, inactive form of the enzyme via
194 formation of a tyrosine radical, yielding the Cu(II)-radical active form. The latter will oxidize an alcohol
195 into the corresponding aldehyde followed by regeneration of the active form via the two-electron
196 reduction of O_2 into H_2O_2. **(B)** *Cor*AlcOx oxidation rate of benzyl alcohol in presence of varying
197 amounts of HRP or *Cor*Perox. **(C)** Activity of *Cor*Perox-*Cor*AlcOx on crude extract of cucumber waxes
198 and derived long-chain aliphatic alcohols, monitored via the production of chromogenic resorufin (RF),
199 product of the Perox-catalyzed oxidation of Amplex-Red by H_2O_2, the latter being the co-product of
200 AlcOx-catalyzed oxidation of primary alcohols into aldehydes. **(D)** EPR spectra of inactive *Cor*AlcOx
201 before (orange curve) and after mixture with *Cor*Perox (black curve). EPR parameters of the Cu(II)
202 inactive form: $g_z = 2.270$, $A_z^{Cu} = 171 \ 10^{-4}$ cm^{-1}, $g_x = 2.047$, $A_x^{Cu} < 50 \ 10^{-4}$ cm^{-1}, $g_y = 2.054$, $A_y^{Cu} < 50 \ 10^{-4}$
203 cm^{-1} and super-hyperfine coupling constant corresponding to two N-ligands $A^N = 43 \ 10^{-4}$ cm^{-1}. **(E)**
204 Lowest energy *Cor*AlcOx-*Cor*Perox complex obtained by protein-protein modeling simulation with
205 PELE (see **fig. S6** for more details). The copper atom is shown as a blue sphere, the heme group as
206 magenta sticks and calcium ions as purple spheres.

The Perox-AlcOx pair gates plant penetration

To investigate the role of the Perox-AlcOx pair in plant infection, we isolated single and double gene deletion mutants of *C. orbiculare* (**fig. S8**). Inoculation of spore suspensions onto intact cucumber cotyledons showed that fewer and smaller lesions were formed by all the mutants compared to the wild-type strains (**Fig. 3A and B**). For instance, the proportion of lesions with a diameter > 4 mm fell from 95 % to < 20%. Furthermore, similar phenotypes were obtained for single and double mutants, suggesting that both oxidases are crucial for fungal pathogenicity.

Further investigations indicated that neither single nor double *perox/alcox* deletion mutants were affected in mycelial growth (**fig. S8A**). Microscopy revealed that the significant loss of pathogenicity of the mutants was due to a large decrease in the frequency of host penetration (**Fig. 3C**). However, morphogenesis, cell wall melanization, and turgor build-up within appressoria cells were virtually indistinguishable from those of the wild-type strain (**fig. S8B-D**). The next step in the infection process is the emergence of a needle-like penetration peg through a pore in the basal cell wall of the appressorium (**Fig. 1A**), during which actin assembly at the pore provides rigidity (*38*). Using a red fluorescent protein/actin-binding protein fusion (Lifeact-RFP), we found normal actin assembly at the appressorium pore for both the single and double mutants inoculated onto cucumber cotyledons (**fig. S8E and F**).

Remarkably, the mutants could penetrate and form hyphae inside inert cellophane membranes (**fig. S9A-C**) and caused wild-type-like lesions when inoculated on mechanically wounded cucumber cotyledons (**Fig. S9D and E**), in contrast to the crippled invasive capacity observed on intact cotyledons (**Fig. 3C**). This points to a mechanism involving plant surface compounds, concordant with the catalytic activity of the Perox-AlcOx pair (**Fig. 2C**). These results collectively indicate that *Cor*AlcOx and *Cor*Perox play a crucial role during the early penetration stage, but are not involved in either appressorium or peg formation.

To further examine the function of the Perox-AlcOx pair during plant infection, we attempted to localize the proteins by live-cell imaging of *Cor*AlcOx-mCherry and *Cor*Perox-GFP driven by their native promoters. Although the *Cor*AlcOx-mCherry and *Cor*Perox-GFP complemented the defect in pathogenicity of the deletion mutants, fluorescence of *Cor*AlcOx-mCherry and *Cor*Perox-GFP was not detectable during appressorium formation on cucumber cotyledons (**fig. S10A**), suggesting that gene expression was too low, consistent with transcriptomic data (**Fig. 1C**), or that the gene products were secreted and diffused away from the penetration site. However, the constitutive overexpression of *Cor*AlcOx-mCherry and *Cor*Perox-GFP, driven by the *translation elongation factor (TEF)* promoter, revealed that both proteins accumulated specifically at the appressorial penetration pore and that signal intensity increased during penetration peg formation (**Fig. 3D**, **fig. S10B and C,** and **Supplementary Movie 1**). This protein co-localization observed *in vivo* is consistent with gene co-expression data (**Fig. 1C**) and rationalizes the co-operative activity demonstrated by biochemical assays (**Fig. 2**). Remarkably, *Cor*AlcOx-mCherry and *Cor*Perox-GFP were detected at the plant surface beneath detached appressoria, at the penetration site (**Fig. 3E**), suggesting that the tandem metalloenzymes are secreted from appressoria into the plant epidermis. Strikingly, *Cor*AlcOx-mCherry and *Cor*Perox-GFP were not detected at the penetration site on cellophane membranes (**fig. S10D**), suggesting that interaction of the fungus with the plant surface triggers local and specific recruitment of the tandem metalloenzymes to the pore.

8

To probe the presence of potential natural substrates of the fungal AlcOx in the neighborhood of the penetration site, we carried out a compositional analysis of waxes present at the surface of uninoculated cucumber cotyledons (**fig. S11**). This analysis showed that the extracted waxes are mainly composed of odd-numbered alkanes (C27-C33) and even-numbered long-chain primary alcohols (C24-C32). Fatty aldehydes were found only as traces. Thus, this experiment demonstrates that potential substrates of AlcOx represent a major part of the plant cuticular compounds while AlcOx reaction products are very minor components.

To further explore the role of Perox-AlcOx in the fungus-plant dialogue, we exposed the *C. orbiculare* single and double mutants to a product of the AlcOx, *viz.* the aliphatic long chain aldehyde *n*-octadecanal. For all gene deletion mutants, the addition of *n*-octadecanal partially restored appressorium penetration ability and lesion formation on cucumber leaves (**Fig. 4A and B**), suggesting that the role of the fungal Perox-AlcOx pair is to generate long chain aldehydes to prime the fungus for efficient plant infection.

Taken together, our results suggest that the role of the fungal Perox-AlcOx pair is to increase locally the concentration of long-chain aldehydes. These aliphatic compounds, members of the volatile organic compounds, are well-known to function as signal molecules (*39*), raising the possibility that the Perox-AlcOx pair generates signals to prime the fungus for efficient plant infection.

To gain insights into the possible steps controlled by the Perox/AlcOx activities during the early infection process, we performed comparative transcriptomic analyses of *C. orbiculare* wild-type and double mutant strains at the appressorial stage on cucumber leaves and cellophane (**Fig. 5**). Analysis of the differentially-expressed genes suggested that the Perox-AlcOx pair contributes to the regulation of a subset of 32 plant-inducible genes predicted to encode small secreted proteins (SSPs), carbohydrate-active enzymes (CAZymes) and membrane transporters (**Table S6**). SSPs and CAZymes are well-known fungal effectors playing a key role in the molecular dialog with host plants. A phylogenetic analysis of CAZymes (**Table S6**) present in this subset of genes revealed that the pair is required for the up-regulation of genes encoding proteins directed towards the plant cell wall (PCW) and the fungal cell wall (FCW) (**Fig. 5**). Among the former, we detected cellulose-active enzymes known to display an enzymatic interplay – *viz.* the cello-oligosaccharide dehydrogenase AA7 and the lytic polysaccharide monooxygenase (LPMO) AA9 (*40*) – as well as pectin-active enzymes from the PL1, PL3 and GH93 CAZy families. Regarding the FCW-targeting proteins, we detected three proteins with carbohydrate binding modules (CBM50s; also called LysM domains) that bind to chitin and function to evade recognition by host immune receptors during infection (*41*).
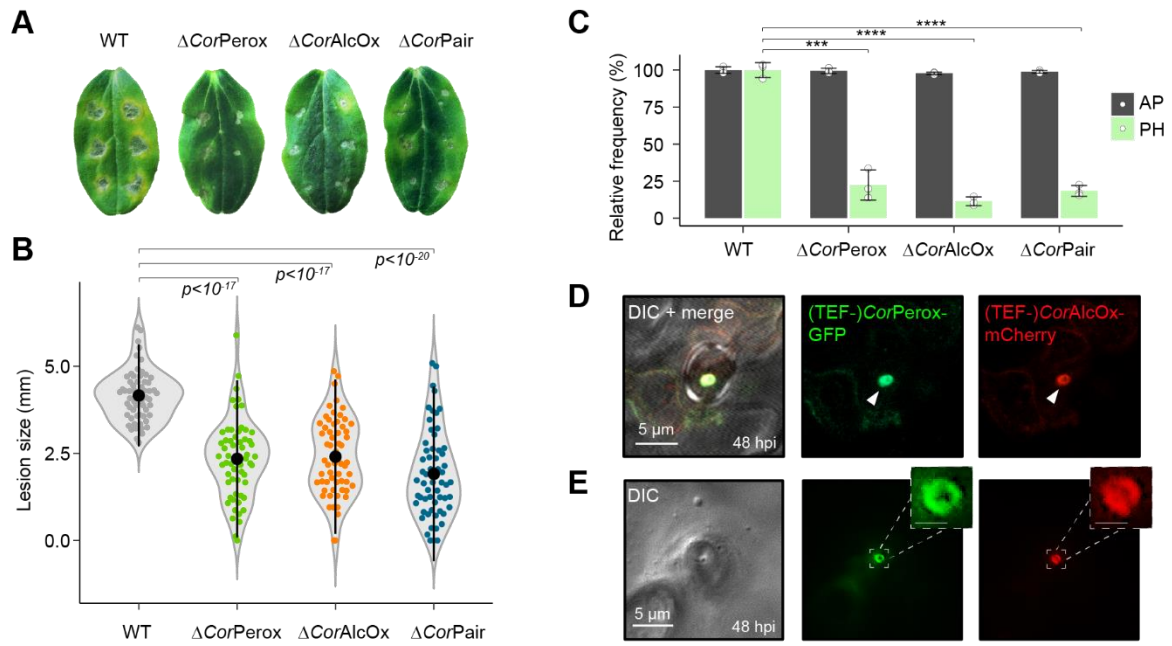
Fig. 3. *In vivo* **characterization of the role of the Perox-AlcOx pair during plant infection. A-B**, Infection phenotypes (**A**) and violin plot of the necrotic lesions size (**B**), at 5 dpi, for the wild-type (WT) and *perox/alcox* deletion mutants of *C. orbiculare* on intact cucumber (*Cucumis sativus*) cotyledons. For each strain/plant combination, at least 60 inoculations were carried out. (**C**) Relative frequency (WT set to 100%) of development of normal appressorium (AP) and penetrating hyphae (PH) by *C. orbiculare* strains on cucumber cotyledons. Data are presented as average values (>300 appressoria for each replicate, n = 3 independent biological replicates) and error bars show s.d.. (**D-E**) Localization of the *C. orbiculare* tandem oxidases on cotyledons at 48 hpi, in the presence of appressoria cells (**D**) or after detachment of the appressoria from the surface of the leaf (**E**). See **movie S1** for a 3D view. In panel **D**, white arrowheads indicate enzyme accumulation at the appressorium pore. In panel **E**, enlarged insets show a ring-like localization of the enzymes (scale bar = 1 µm). In panels **B-C**, a one-tailed independent *t*-test for each mutant *vs* WT was applied (***$P<0.001$, ****$P<0.0001$).
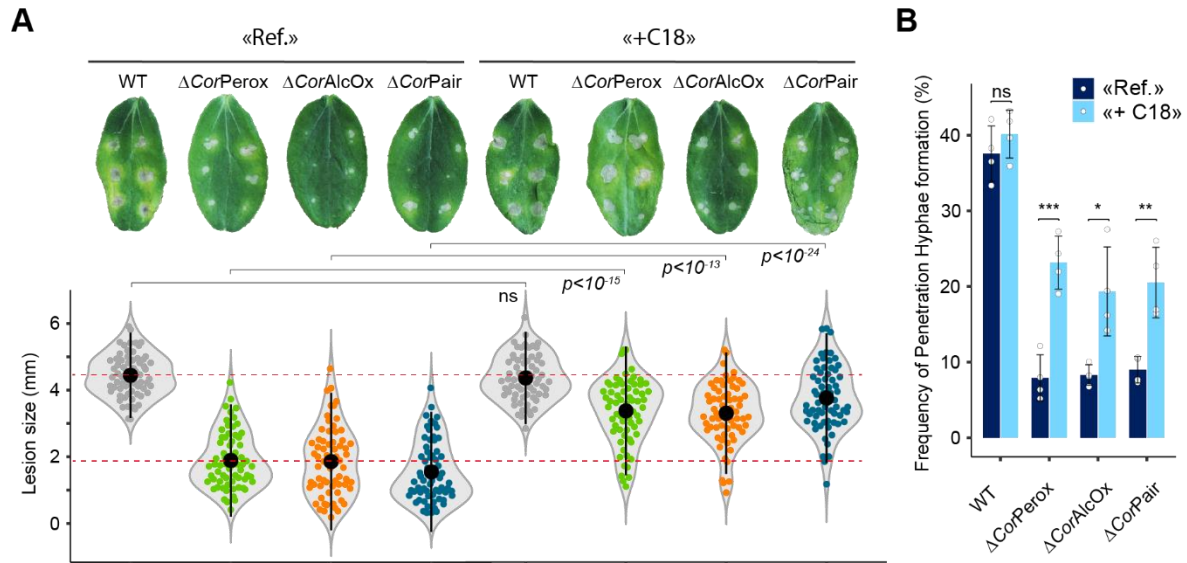
Fig. 4. Effect of *n*-octadecanal on the pathogenicity of *perox/alcox* deletion mutants. The figure shows the effect of the addition of 10 μM *n*-octadecanal (denoted as +C18) on necrotic lesions size formed by *C. orbiculare* WT and mutant strains on cucumber cotyledons (24°C, 5 days) (**A**) and on the formation of penetration hyphae (**B**). Control experiments, i.e. 1% ethanol without addition of *n*-octadecanal, are denoted as Ref. In panel **A**, for each strain, we show one representative cotyledon image of the infection phenotype and, below, a violin plot of lesions sizes based on 66 inoculation sites per condition (carried out over 4 independent biological replicates). In panel **B**, data are presented as mean percentages (>300 appressoria per replicate, n = 4 independent biological replicates) and error bars show s.d. In panels A and B, for each strain, a one-tailed independent *t*-test of +C18 *vs* Ref was applied.
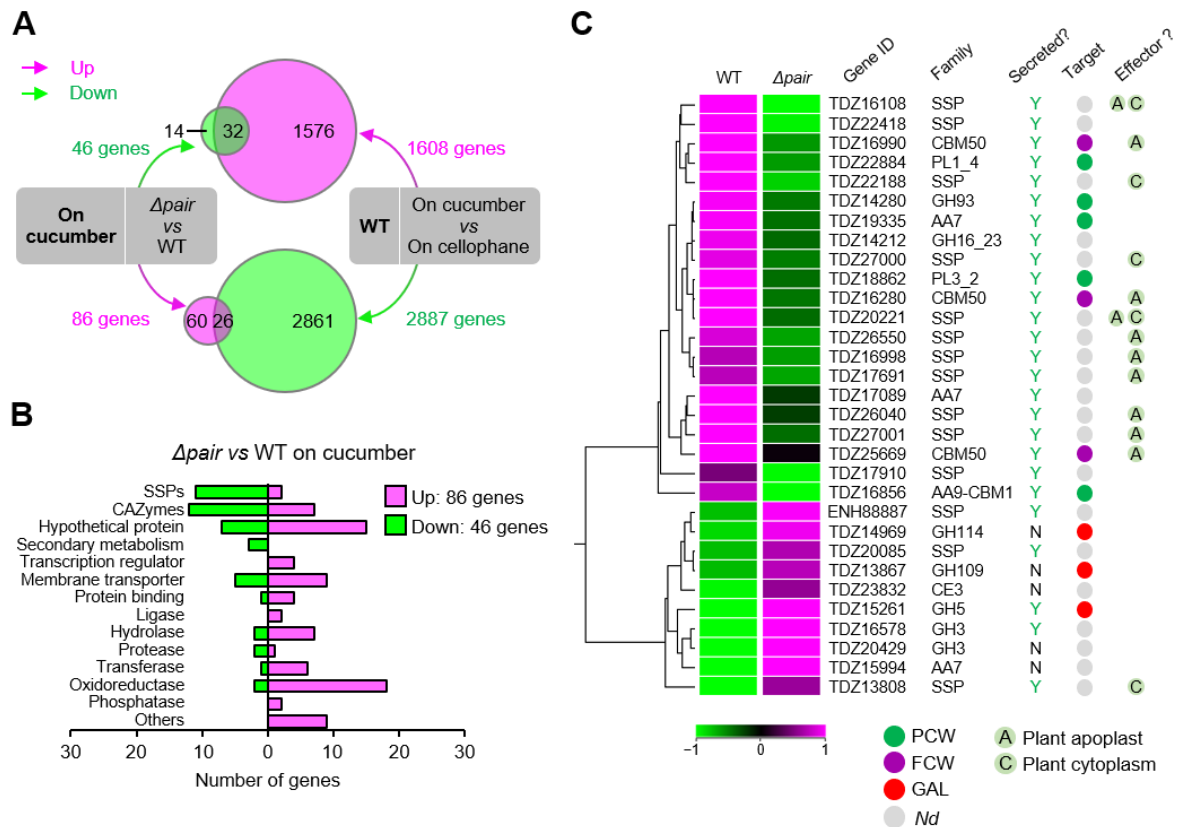
315

Figure 5. Loss of the Perox-AlcOx pair affects fungal gene expression during appressorium-mediated penetration of *C. orbiculare*. (A) Venn diagrams illustrating the differentially regulated (up-or down-regulated) genes between cucumber *vs* cellophane that are under control of the AlcOx-Perox pair. **Top**: green circle indicates the number of downregulated genes (46 genes) in *Δpair* compared with wild-type strain (WT), both incubated on cucumber; magenta circle denotes the number of genes (1608 genes) upregulated on cucumber *vs* cellophane in the WT strain. **Bottom**: Magenta circle indicates the number of upregulated genes (86 genes) in *Δpair* compared with WT, both incubated on cucumber; green circle shows the number of downregulated genes (2887 genes) in the WT strain on cucumber vs cellophane. In the top and bottom Venn diagrams, the overlap indicates that 32 and 26 genes are respectively upregulated or downregulated in the presence of the plant and also under control of the AlcOx-Perox pair. **(B)** Class-wise distribution of the number of genes that were differentially expressed in appressoria of the *Δpair* double mutant compared with WT on cucumber cotyledons. **(C)** Hierarchical clustering heatmap of differentially expressed genes encoding CAZymes and SSPs in the *Δpair* mutant compared to WT on cucumber cotyledon. The expression values per gene were median normalized. The columns were clustered by Euclidean distance. The expression levels of up- (magenta) and down-regulated (green) genes are shown as log2-transformed values. On the right-hand side of the figure, we show the presence of a predicted signal peptide (Y, Yes; N, No), phylogeny-based substrate specificity predictions for CAZymes (PCW, plant cell wall; FCW, fungal cell wall; GAL, galactose-containing compounds; *Nd*, not determined) and SSPs/CBM50s that are putative effectors (pale green circles) predicted to localize in the plant cell (in the apoplast (A) and/or the cytoplasm (C)). See **Table S6** for more details.

337

Discussion

Research on plant invasion by appressorium-forming fungi teaches us that the development of these specialized infection structures is an extremely complex, finely regulated process. In this study, we have shown that fungal AlcOx, which are only encountered in phytopathogens, have a very different biological function than the few distantly-related CROs for which roles in morphogenesis (*42*, *43*) or lignin degradation (*18*) were proposed. We showed that the tandem Perox-AlcOx metalloenzymes are specifically deployed at the initiation of penetration peg formation and their localization at the pore formed at the fungus-plant cell interface. Our results suggest that the oxidative action of Perox-AlcOx on long-chain alcohols triggers a yet-to-be-elucidated biochemical cascade leading to penetration. Indeed, functional complementation of the deletion mutants, which were defective in their ability to puncture intact plant cuticles, by the product of the reaction suggests that cuticular alcohol oxidation provides a chemical cue required for plant cell entry (**Fig. 6**). We speculate that acquisition of the Perox-AlcOx pair provided the ecologically widespread *Colletotrichum* and *Magnaporthe* species with an advantage, namely an *in-house* "locksmith" (i.e. the tandem metalloenzymes) ensuring localized production of the aldehyde. This entry key is needed to move to the next pathogenesis stage with the expression of PCW–degrading enzymes to facilitate penetration, and of FCW-binding proteins and carbohydrate oxidases to evade host immunity. For example, it has been suggested that, upon oxidation by fungal LPMOs and oligosaccharide oxidases, plant oligosaccharides can no longer play their role as inducers of host immune response (*40*, *44*, *45*).

It is interesting to speculate why Nature has evolved such a complex enzymatic system relying on heme-iron peroxidase and elaborate copper radical chemistry when simpler, mono-enzyme systems could be employed for the same purpose (e.g. FAD-dependent oxidases active on long-chain alcohols (*46*)). We show that the functional integrity of the secreted tandem metalloenzymes system endows pathogenic fungi with fine control over oxidation reactions in the extracellular space. We propose that the copper-radical center equips CROs with a "redox switch" to turn on activity with high spatio-temporal resolution, when paired with a cognate peroxidase (**Fig. 6**). More generally, our study suggests that fungi have evolved ways of controlling oxidative reactions that are seemingly out of reach, i.e. beyond the bounds of the fungal plasma membrane and cell wall, through tight genetic regulation and protein interplay between secreted oxidoreductases.

In conclusion, using a combination of *in silico*, *in vitro* and *in vivo* approaches, we have unveiled the existence of a natural redox partner, i.e. a heme-peroxidase, for AlcOx-type CROs, and showed that the pair acts as a secreted virulence factor during early infection (**Fig. 6**). It is noteworthy that the enzymology-driven approach pursued here was essential to bring to light this unique mechanism, because low expression levels, fine temporal tuning, and highly localized co-secretion of the Perox-AlcOx would have evaded classical 'omic approaches. The specific occurrence of the Perox-AlcOx pair in most *Colletotrichum* and *Magnaporthe* species raises the possibility that functionally equivalent, coupled oxidative enzymatic mechanisms may operate in other appressorium-forming fungal pathogens. We anticipate that the present discovery will open new research avenues, notably on the role of wax-derived compounds in the cascade of events leading to successful infection as well as on the development of oxidase-specific inhibitors as surface-acting, anti-penetrant drugs for crop protection.

13

382
383
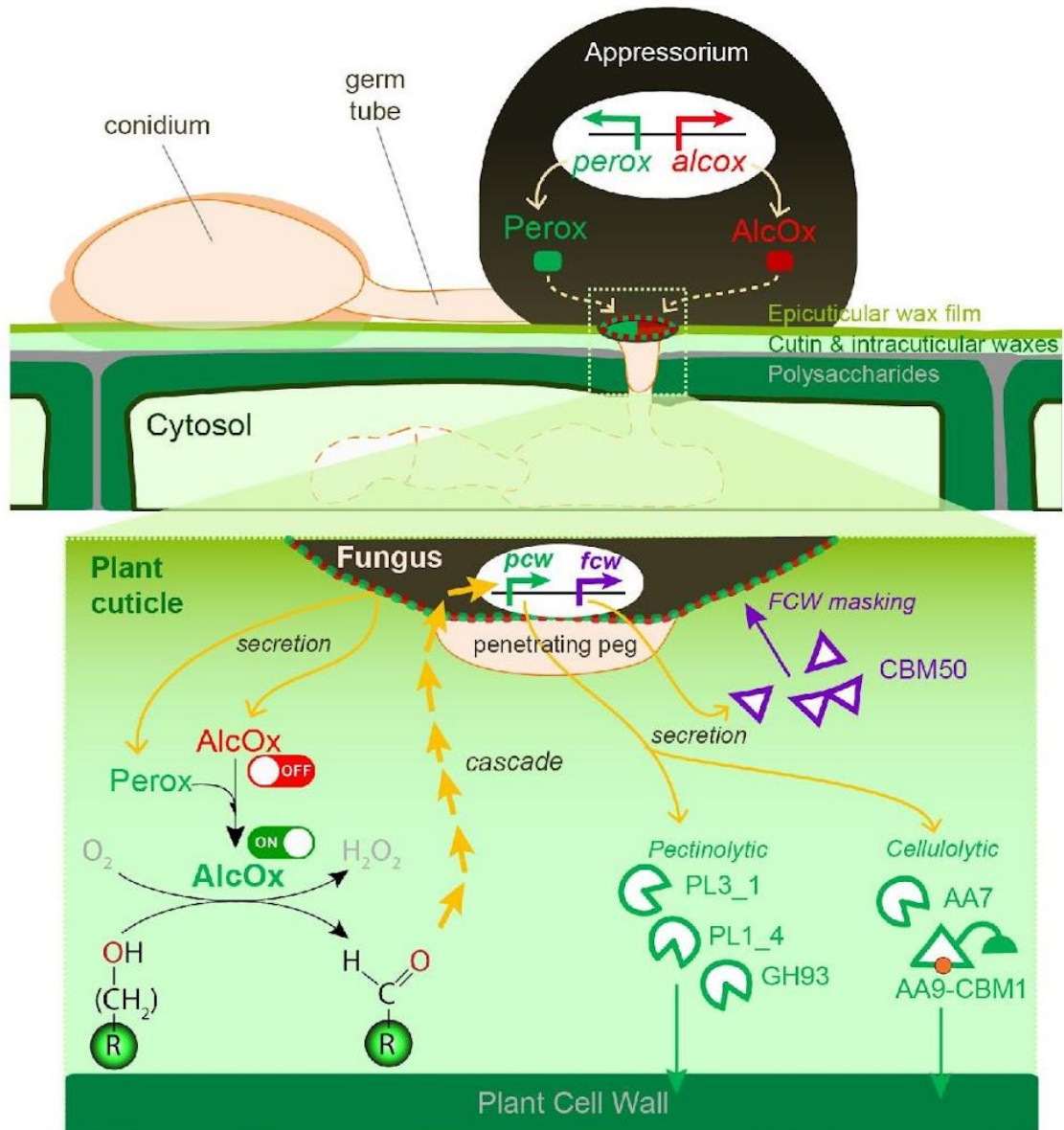
384
385
386
387 **Fig. 6. Schematic summary of the recruitment of the fungal Perox-AlcOx pair during early plant**
388 **penetration and its proposed role in the induction of a biochemical cascade.** The bottom panel is a
389 zoom-in view illustrating the Perox-AlcOx reaction occurring at the fungus-plant interface and the
390 triggered downstream cascade, highlighting the induction of genes encoding proteins targeting the plant
391 cell wall (*pcw*) and fungal cell wall (*fcw*).
392

Materials and Methods

Chemicals and commercial enzymes

Most chemicals were purchased from Sigma (Darmstadt, Germany) or VWR (Fontenay-sous-Bois, France) unless stated otherwise. Molar concentrations of type II HRP (Sigma-Aldrich; MW 33.89 kDa) were estimated by Bradford assay. *n*-octadecanal was purchased from TCI-Europe (Zwijndrecht, Belgium). All alcohol substrates stock solutions were prepared either in H_2O or in acetone and stored at -20°C. The concentration of H_2O_2 stock solution was verified at 240 nm ($\varepsilon^{240} = 43.6$ $M^{-1}.cm^{-1}$).

Bioinformatics

Species tree of the 18 ascomycete genomes (shown in **Fig. 1b**) was constructed as previously described (*47*). Core clusters containing only one protein-coding gene per species were identified using FastOrtho (*48*) with the following parameters: 50% identity and 50% coverage. Each cluster was aligned with MAFFT 7.221 (*49*), and curated alignments were concatenated with Gblocks 0.91b (*50*). The tree was finally constructed with RAxML 7.7.2 (*51*) (PROTGAMMAWAG model and 500 bootstrap). Phylogenetic analysis of AA5_2 genes and «standard» haem peroxidases (PFAM 00141, including Class II peroxidases) from 30 *Colletotrichum* genomes relied on 72 and 333 sequences, respectively (see **fig. S2** legend and **Table S3** for more details). The phylogenetic analysis of the peroxidase-catalase superfamily relied on 150 sequences encompassing Class I (intracellular peroxidases), II (fungal secreted peroxidases) and III (plant secreted peroxidases) peroxidases and from so-called Hybrid B peroxidases, as previously reported (*52*). Subsequently to manual curation (removing signal peptides), the sequences were first aligned using MAFFT-DASH (L-INS-i method) (*53*) and the resulting multiple sequence alignment (MSA) was used to infer a phylogenetic tree using RAxML (1000 bootstraps). The trees were then visualized in iTOL (*54*) and edited in Illustrator®.

For the gene neighborhood survey, we retrieved 4 genes located upstream and downstream of each *Colletotrichum*'s AA5_2 query (72 sequences). The resulting 569 genes were assigned to 78 different PFAM domains. The frequency of occurrence of a given type of domain in the neighborhood of each AA5_2 phylogenetic clade was then computed and visualized in Excel. For interrogating the co-occurrence of both Perox and AlcOx-coding genes beyond *Colletotrichum* species two independent BLAST searches were run against the NCBI non-redundant database, using *Cor*AlcOx and *Cor*Perox as query sequences. 1,000 AlcOx-like (down to 37% sequence identity) and 1,000 Perox-like (25% sequence identity) sequences along with their corresponding source microorganism were retrieved. A cross-comparison of both lists of microorganisms, applying different sequence identity-based thresholds (60% for AlcOx and 30% for Perox) returned the list of species harboring both type of enzymes.

Transcriptomics data were retrieved from publicly available datasets (*26–29*). To normalize different dataset longitudinally, we expressed reported sampling time points as infection stages in Fig. 1 as follows (hpi = hours post-infection): for *C. fructicola nara gc5/strawberry* (*27*), AP (24 hpi), BP (72 hpi) and NP (144 hpi); for *C. orbiculare/N. benthamiana* (*27*), AP (24 hpi), BP (72 hpi) and NP (168 hpi); for *C. higginsianum/A. thaliana* (*26*), AP (22 hpi), BP (40 hpi) and NP (60 hpi); *C. graminicola/Maize* (*26*), AP (22 hpi), BP (40 hpi) and NP (60 hpi);

15

437   *M. oryzae/Rice* (*28*), AP (8 hpi), BP (24 hpi) and NP (48 hpi); *M. oryzae/Barley* (*29*), AP (12

438   hpi), PP (24 hpi), BP (36 hpi) and NP (48 hpi).

439

440   **Structure Prediction and Preparation**

441   *Surface hydrophobicity*

442   Structural homology models were generated with AlphaFold (*55*) and surface hydrophobicity

443   of selected CROs was computed with the "protein-sol patches" online software (*56*). Average

444   hydrophobicity of the binding surface was determined as follows: using PyMOL 2.4, we

445   selected the residues constituting the entire binding surface of *Fgr*GalOx, *Cgr*AlcOx and

446   equivalent residues (based on MSA) in orthologous enzymes (5 GalOx and 11 AlcOx in total)

447   as well as those of 4 characterized hydrophobins (PDB 2N4O, 2LSH, 1R2M and 2FZ6) as

448   hydrophobic protein reference. Average hydrophobicity of the selected residues was computed

449   as a GRAVY index score (Kyte-Doolittle method) (*57*).

450   *Preparation of models for docking experiments*

451   We used Alphafold2 (*55*) to obtain a model for *Cor*AlcOx and *Cor*PerOx. To add the metals

452   and cofactors to AlphaFold2 models, we performed a BLAST search in the Protein Data Bank

453   proteins database and selected the PDB 2EIC (Sequence Identity 47%) to add the copper to

454   *Cor*AlcOx, and the PDB 1MN2 (Sequence Identity 28%) to add the calcium ions and the heme

455   group to *Cor*Perox. Subsequently, we prepared the systems with Schrödinger Protein

456   Preparation Wizard (*58*) to determine the protonation states at pH 7 using PROPKA (*59*), and

457   finally relax the systems performing a restrained minimization with convergence criteria for

458   heavy atoms to 0.30 Å using the OPLS_2005 force field.

459   *Protein-Protein Docking*

460   For the generation of protein-protein poses (PPPs), we used PIPER (*35*) to generate 70,000

461   PPPs, which were clustered with the in-built clustering protocol using the default RMSD

462   threshold of 9.0 Å and a minimum population of 10 poses per cluster. In parallel, we also used

463   the recently developed Alphafold2 Multimer (*36*), which only uses sequence information,

464   together with ion and cofactor placements, as described above.

465   *PPPs refinement with PELE*

466   We used the all atom Monte Carlo (MC) software PELE (Protein Energy Landscape

467   exploration), to map intermolecular interactions (*37, 60*). PELE follows a heuristic MC

468   approach, generating new conformational proposals using vibration modes of the proteins with

469   translations and rotations of the ligand (*Cor*Perox in this case), and relaxing the system with

470   structure prediction methods, so that the probability of acceptance in the Metropolis criterion

471   (*61*) remains high (*60*). Here, we refined the top five PIPER and five AlphaFold2-Multimer

472   models, using a simulation of 250 PELE steps with 256 computing cores (about 25 independent

473   trajectories per model). Each MC PELE step consists of a perturbation and a relaxation stage.

474   In the first one, a perturbation of the ligand, *Cor*AlcOx in this case, is first performed, including

475   random rotations of 0.01-0.04 rad and translations of 0.25-0.50 Å, and is followed by a

476   backbone perturbation of both proteins following the normal modes directions predicted by an

477   Anisotropic Network Model (ANM). In the second stage, the system is first relaxed by a high

478   resolution side chain prediction including all protein-protein interphase side chains, defined by

479   the region within 3 Å of any heavy atom of the other protein. Afterwards, a global minimization

480   is performed to relax the entire system, providing a final conformation and energy; this energy

481   is then used in a Metropolis importance sampling to accept/reject the MC step.

482   *Exploring the substrate interactions*

483   The C18 substrate was created with Maestro 3D Builder, followed by a Glide docking (*62*) on

484   the lowest energy PPPs, as predicted with PELE. The docking grid was defined with a cubic

485   box of 30 Å centered in between the copper ion and Tyr120(OH) of the *Cor*AlcOx. Following

486   the Glide rigid receptor docking, we performed a C18 induced fit rescoring simulation

487   involving 40 PELE steps (using 48 computing cores). Each PELE step consisted of a random

488   rotation of 0.01-0.04 rad and translation of 0.05-0.15 Å, using a spherically restrained search

489   space of radius 12 Å centered on the copper ion. The perturbation step was then followed by a

490   relaxation phase including side chain prediction (all side chains inside the spherical space) and

491   a full system minimization.

492

493   **DNA cloning and strain production**

494   DNA cloning and strain production of the AA5_2 alcohol oxidases (AlcOx) from

495   *Colletotrichum graminearum* (*Cgr*AlcOx, Genbank ID XM_008096275.1, Uniprot ID

496   E3QHV8) was already carried out in previous study (*19*). The intron-free sequences of the

497   genes coding for the AlcOx from *Colletotrichum orbiculare* MAFF 240422 (*Cor*AlcOx,

498   Genbank ID TDZ17043.1, Uniprot ID N4UTF2), the AlcOx from *Magnaporthe oryzae*

499   (*Mor*AlcOx, Genbank ID XM_003719321.1, Uniprot ID G4NG45), the Tandem Peroxidase

500   (Perox) from *Colletotrichum orbiculare* (*Cor*Perox, Genbank ID TDZ17044.1, Uniprot ID

501   N4UUY4) and the Tandem Peroxidase from *Magnaporthe oryzae* (*Mor*Perox, Genbank ID

502   XM_003719322.1, Uniprot ID G4NG46) were synthesized after codon optimization for

503   expression in *P. pastoris* and inserted into a modified pPICZαC vector using *Xho*I* and *Not*I

504   restriction sites in frame with the α secretion factor at N-terminus (i.e. without native signal

505   peptide) and with a (His)$_6$-tag at the C-terminus (without *c*-myc epitope) (Genewiz, Leipzig,

506   Germany). Transformation of competent *P. pastoris* X33, selection of zeocin-resistant

507   *P. pastoris* transformants screened for protein production was carried out as described by Haon

508   et al. (*63*). The best-producing transformants were conserved as glycerol stock at – 80°C.

509

510   **Heterologous protein production in flasks**

511   All proteins were first produced in 2 L Erlenmeyer flasks. To this end, single colonies of *P.*

512   *pastoris* X33 expressing each gene of interest were individually streaked on a YPD agar plate

513   containing Zeocin (100 μg.mL^{-1}) and incubated 3 days at 30°C. A single colony was then used

514   to inoculate 5 mL of YPD, in a 50 mL sterile Falcon tube and incubated during 5 h (30°C, 160

515   rpm). This pre-culture was used to inoculate at 0.2% (vol/vol) 500 mL of BMGY medium, in

516   a 2 L Erlenmeyer flask, incubated during approximately 16 h (30°C, 200 rpm) until the OD_{600}

517    $_{nm}$ reached 4−6. The produced cellular biomass was then harvested by centrifugation (5 min,

518   16°C, 3,000 x *g*). For the AlcOx, the cell pellet was then resuspended in 100 mL BMMY

519   medium supplemented with methanol (1%, vol/vol) and $CuSO_4$ (500 μM). The culture was

520   incubated for 3 days (16°C, 200 rpm), with daily additions of methanol (1% added, vol/vol).

521   The Tandem Peroxidases production conditions were optimized and varied from the standard

protocol as follows: the BMMY was supplemented with methanol (3% vol/vol), hemin (25 µM) and CaCl$_2$ (2 mM). The culture was incubated for 3 days (20°C, 200 rpm), with daily additions of methanol (3%, vol/vol) and hemin (25 µM). Then, the extracellular medium was recovered by centrifugation (10 min, 4°C, 3,000 x g) and the supernatant filtrated on 0.45 µm membrane (Millipore, Massachusetts, USA) and stored at 4°C prior to purification.

Heterologous protein production in bioreactors

The upscaled production of *Cor*Perox was carried out in 1.3 L and 7.5 L bioreactors (New Brunswick BioFlo 115 fermentor, Eppendorf, Germany) as per the *P. pastoris* fermentation process guidelines (Invitrogen) with the following optimizations: the glycerol fed-batch phase was replaced by a sorbitol and methanol transition phase, besides 200 µM (1.3 L bioreactor) and 150 µM (7.5 L bioreactor) of hemin were added to the methanol solution. CaCl$_2$ (10 mM final) was added to the crude protein solution before being either directly purified or flash-frozen in liquid nitrogen and stored at -80°C. We verified that flash-freezing did not cause any activity loss, for both AlcOx and Perox enzymes.

Protein purification

The filtered *Cor*AlcOx and *Mor*AlcOx crude supernatants were adjusted to pH 8.5, filtered on 0.22 µm filters (Millipore, Molsheim, France), and purified by anion exchange chromatography (DEAE) on a HiPrep FF 16/10 column (GE Healthcare, USA). Elution was performed by applying a linear gradient from 0 to 500 mM NaCl (in Tris-HCl buffer 50 mM, pH 8.5) over 20 column volumes, with a flow rate set to 5 mL.min^{-1}.

The filtered *Cor*Perox and *Mor*Perox culture supernatant was adjusted to pH 7.8 just before purification and filtered on 0.22 µm filters (Millipore, Molsheim, France). Depending on the volume to purify, the crude protein sample was either loaded on a His-Trap HP 5-mL column (GE Healthcare, Buc, France) on a HisPrep FF 16/10 column (GE Healthcare) connected to an ÄKTAxpress system (GE Healthcare) equilibrated with HEPES (10 mM, pH 8.0), NaCl (100 mM), CaCl$_2$ (2 mM) and imidazole (10 mM) buffer. Each (His)$_6$-tagged recombinant enzyme was eluted with HEPES (10 mM, pH 8.0), NaCl (100 mM), CaCl$_2$ (2 mM) and imidazole (500 mM) buffer. The Tandem Peroxidases were further purified by size exclusion chromatography, using a HiLoad 26/600 Superdex 200 pg column (GE Healthcare) operated at 2.5 mL/min and with a running buffer containing HEPES (10 mM, pH 8.0), NaCl (100 mM) and CaCl$_2$ (2 mM). After SDS-PAGE analysis, fractions containing the recombinant enzyme were pooled, concentrated and buffer exchanged in sodium phosphate (50 mM, pH 7.0) for the AlcOx or in HEPES (10 mM, pH 8.0), NaCl (100 mM) and CaCl$_2$ (2 mM) buffer for the Tandem Peroxidases.

Protein concentrations of *Cgr*AlcOx (52,337 Da, ε^{280} = 101,215 M^{-1}.cm^{-1}), *Cor*AlcOx (52,317 Da, ε^{280} = 92,735 M^{-1}.cm^{-1}), *Mor*AlcOx (62,894 Da, ε^{280} = 90,020 M^{-1}.cm^{-1}), *Cor*Perox (26,137 Da, ε^{280} = 21,345 M^{-1}.cm^{-1}), and *Mor*Perox (26,290 Da, ε^{280} = 24,450 M^{-1}.cm^{-1}) were determined by the Bradford assay (*64*) using BSA as reference protein as well as by UV absorption at 280 nm using a Nanodrop ND-200 spectrophotometer (Thermo Fisher Scientific, Massachusetts, USA).

Enzyme assays

For screening the substrate specificity of CRO-AlcOx enzymes, the alcohol substrates were prepared in sodium phosphate buffer (50 mM, pH 7.0) in 96-well microplates and reactions were initiated by the addition of a pre-mix of CRO-AlcOx (1 nM final concentration), HRP (0.1 mg.mL^{-1}) and 2,2′-azino-bis(3-ethylbenzothiazoline-6-sulfonic acid (ABTS, 500 μM) in sodium phosphate buffer (50 mM, pH 7.0). The tested substrates included D-glucose (50 mM final concentration, D-Glc), D-galactose (50 mM, D-Gal), D-raffinose (50 mM, D-Raf), xyloglucan (0.1% mM, XG), butan-1-ol (3 mM), butan-2-ol (3 mM), octan-1-ol (3 mM), decan-1-ol (3 mM), 2,4-hexadiene-1-ol (3 mM, HD-OH), glycol aldehyde dimer (3 mM, GAD), benzyl alcohol (3 mM, BnOH), 4-hydroxybenzyl alcohol (3 mM, p-OH BnOH), vanillic alcohol (3 mM, Van-OH), syringic alcohol (3 mM, Syr-OH) and cinnamyl alcohol (3 mM, Cin-OH). The absorbance of the final reaction (100 μL total volume) was monitored at 414 nm using a microplate spectrophotometer (TECAN), thermostated at 23°C. The 414 nm absorbance allows to determine the concentration of ABTS cation radical over time (ABTS$^{•+}$, ε^{414} = 31,100 M^{-1}.cm^{-1}), and in turn the rate of alcohol oxidation, considering a peroxidase reaction stoichiometry for (H$_2$O$_2$:ABTS$^{•+}$) of 1:2 and a CRO-AlcOx reaction stoichiometry for (alcohol:H$_2$O$_2$) of 1:1.

For screening the substrate specificity of *Cor*Perox, unless stated otherwise the enzyme (0.125 μM final) was prepared in citrate-phosphate buffer (50 mM, pH 4.0 to 7.0) in 96-well microplates (for wavelength in the visible range) or in 1 mL Quartz cuvettes (for UV range), in the presence of various substrates (*vide infra*). Reactions were initiated by the addition of H$_2$O$_2$ (100 μM final), incubated at 23°C, and monitored spectrophotometrically at the wavelengths indicated below. The tested peroxidase substrates included: ABTS (500 μM) converted into ABTS$^{•+}$ (ε^{414} = 31,100 M^{-1}.cm^{-1}); 2,6-dimethoxyphenol (2,6-DMP, 500 μM) converted into hydrocoerulignone (ε^{469} = 53,200 M^{-1}.cm^{-1}); guaiacol (500 μM) converted into the final product tetraguaiacol (ε^{470} = 26,600 M^{-1}.cm^{-1}); Reactive Black 5 (RB5, 100 μM, ε^{600} = 20,000 M^{-1}.cm^{-1}) converted into non-chromogenic product RB5^{ox}; veratryl alcohol (500 μM) converted into veratraldehyde (ε^{310} = 9,300 M^{-1}.cm^{-1}). For testing the manganese peroxidase activity, *Cor*Perox was mixed with Mn(II)SO$_4$ (1 mM final) in tartrate buffer (50 mM, pH 2.0 to 5.0) and the formation of Mn^{3+}-tartrate complex upon addition of H$_2$O$_2$ (100 μM) was followed at 238 nm (ε^{238} = 6,500 M^{-1}.cm^{-1}), as previously described (*65*).

All activities were expressed as Vi/E (s^{-1}), i.e. the initial rate (Vi, μmoles of H$_2$O$_2$ consumed per second) divided by the amount of enzyme (in μmoles).

*Cor*Perox stability over time was carried out by monitoring the peroxidase activity of *Cor*Perox samples (50 μM) stored in sodium acetate buffer (50 mM, pH 5.2), at 4°C, in the presence of varying concentrations of CaCl$_2$ (0-500 mM). The peroxidase activity of these samples was measured as described above (final concentration of 0.5 μM *Cor*Perox), using ABTS (500 μM) and H$_2$O$_2$ (100 μM) as substrates, in citrate-phosphate buffer (50 mM, pH 4.0), at 23°C.

Michaelis-Menten kinetic parameters of *Cor*Perox were determined by measuring the peroxidase initial rate, as described above, in the presence of ABTS (500 μM) and varying

607 concentrations of H_2O_2 (0-1200 µM), in citrate-phosphate buffer (50 mM, pH 4.0), at 23°C.
608 Experimental data could be fit to the standard Michaelis-Menten equation (residual standard
609 error = 0.019).
610 AlcOx activation by the peroxidases was assayed by monitoring changes in absorbance at 254
611 nm upon oxidation of benzyl alcohol (1.5 mM) into benzaldehyde by the CRO (10 nM final
612 concentration), in the presence of varying concentrations of peroxidase (0-1000 nM). Reactions
613 were carried out in sodium-phosphate buffer (50 mM, pH 7.0), at 23°C, in UV-transparent
614 cuvettes (1 mL reaction volume). The reactions were initiated by addition of the CRO and
615 vigorously mixed by pipetting up and down. The absorbance was measured using an Evolution
616 201 UV-Vis spectrophotometer (Thermo-Fisher). The concentration of benzaldehyde was
617 calculated as $[\text{Benzaldehyde}]_t = (\text{Abs}^{254\ nm}_t - \text{Abs}^{254\ nm}_{t0})/(\varepsilon^{254}_{benzaldehyde} - \varepsilon^{254}_{BnOH})$, where
618 $\varepsilon^{254}_{benzaldehyde} = 8,500\ M^{-1}.cm^{-1}$ and $\varepsilon^{254}_{BnOH} = 150\ M^{-1}.cm^{-1}$.
619

Gas chromatography (GC) analysis

621 Enzymatic reactions were carried out in 4 mL-clear borosilicate glass vials closed by screw
622 caps with PTFE septum (500 µL final reaction volume). *Cor*AlcOx (2 µM final) was mixed
623 with *Cor*Perox (2 µM) in sodium phosphate buffer (50 mM, pH 7.0). The reaction was initiated
624 by the addition of octadecanol (0.3 mg.mL^{-1}, eq. 1.1 mM final) and the mixture was incubated
625 at 23°C at 190 rpm in an Innova 42R incubator (New Brunswick, USA), during 1 h. Following
626 a previously published protocol (*22*), the reaction mixture was then acidified by addition of 10
627 µL HCl (12 M). Products and possible remaining substrate were extracted by adding 500 µL
628 of hexane (containing 1 mM of internal standard dodecane), followed by shaking and
629 centrifugation for 5 min at 3,000 x *g*. The organic layer was transferred into a new vial and
630 analyzed with a GC-2010 Plus apparatus (Shimadzu, Japan) equipped with a flame ionization
631 detector (FID) and a DB-5 capillary column (30 m x 0.25 mm x 0.25 µm; Agilent). Nitrogen
632 (200 kPa) was used as carrier gas. The injector and detector temperatures were set at 250°C.
633 After injection (2 µL sample), the analytes were separated by applying the following
634 temperature program: step 1) from 65°C to 250°C over 9.25 min (i.e. 20°C/min); step 2) plateau
635 at 250°C for 6 min. For quantitation, standard curves of octadecanol, *n*-octadecanal and
636 octadecanoic acid were prepared by following the same procedure.
637

Electron Paramagnetic Resonance (EPR)

639 EPR spectra were recorded on frozen solutions (120K) using a Bruker Elexsys E500
640 spectrometer operating at X-band equipped with a BVT 3000 digital temperature controller.
641 The following acquisition parameters were used: modulation frequency 100 kHz; modulation
642 amplitude 5 G; gain 87 dB; and microwave power, 20 mW. EPR spectra were simulated using
643 the EasySpin toolbox developed for Matlab (*66*). *Cor*AlcOx (100 µM final), prepared in
644 sodium phosphate buffer (50 mM, pH 7.0), in the absence or presence of *Cor*Perox (100 µM
645 final), was flash-frozen in liquid nitrogen and continuous-wave EPR spectra were recorded.
646 *Cor*AlcOx and *Cor*Perox were placed in contact for various amount of time (2.5 min, 15 min)
647 before flash-freezing the solution. Controls containing buffer only or the *Cor*Perox were also
648 carried out.
649

Analysis of cuticular waxes from cucumber cotyledons

Cuticular waxes were extracted from 2-weeks old cotyledons by immersing 6 intact cotyledons for 30 s in chloroform in a glass beaker. Chloroform was evaporated under a stream of nitrogen gas and wax extracts were derivatized using N,O-Bis (trimethylsilyl)trifluoroacetamide (BSTFA) and analyzed by gas chromatography coupled to mass spectrometry (GC-MS) as previously described (*67*).

Strains and media

Strain 104-T (MAFF240422) of *C. orbiculare* was used as the wild-type strain. All strains used in this study are listed in **Table S4** (*13*, *38*, *68–70*). *C. orbiculare* strains were cultured on 3.9% PDA (Nissui) at 24°C in darkness. For genetic manipulation, *Escherichia coli* DH5α-competent cells were maintained on Luria-Bertani (LB) agar at 37°C. For fungal transformation, *Agrobacterium tumefaciens* C58C1 was maintained on LB agar at 28°C. Transformations of *C. orbiculare* (*13*, *38*) were carried out as previously described.

Strain construction

Primers and plasmids used in this study are listed in **Table S5**. For construction of *CorAlcOx* deletion strains, 1.1-kb upstream and 1.0-kb downstream flanking sequences and a 1.0-kb fragment of the neomycin-resistance cassette was amplified with the respective primer pairs. For construction of *CorPerox* deletion strains, 1.1-kb upstream and downstream flanking sequences and a 1.4-kb fragment of the hygromycin-resistance cassette was amplified. These three fragments were inserted into linearized pPZP-PvuII using the In-Fusion HD cloning kit (Clontech). The same procedures were used for construction of *M. oryzae* gene deletion strains. For construction of *CorAlcOx-mCherry* and *CorPerox-GFP* gene fusion, a 5.9-kb *CorAlcOx-CorPerox* fragment containing 1.1-kb downstream flanking sequences was inserted into linearized pPZP-PvuII-SUR, and the mCherry and GFP fragments were inserted.

For construction of *CorAlcOx-mCherry* overexpression strains, a 4.0-kb *CorAlcOx-mCherry* fragment containing its 1.1-kb downstream flanking sequence was amplified from pPZP-AlcOx-mCherry-Perox-GFP-S, and fused to linearized pCAMSUR-TEF (*71*) containing the translation elongation factor promoter of *Aureobasidium pullulans* (*72*). The same procedures were used for construction of *CorPerox-GFP* overexpression strains.

Plant infection

Infection assays on detached cucumber leaves (*Cucumis sativus* L. 'Suyo') with conidial suspension (1×10^5 conidia/ml in distilled water) of *C. orbiculare* were performed as previously described (*73*). The inoculated leaves were incubated in a humid environment for 5 days at 24°C. For testing the effect of *n*-octadecanal supplementation, conidial suspensions (1×10^5 conidia/mL in 10 μM *n*-octadecanal dissolved in 1% ethanol or 1% ethanol as a control) were spotted onto detached cucumber leaves, and incubated in a humid environment for 5 days at 24°C.

Microscopy

For observation of appressorium formation of *C. orbiculare*, a conidial suspension (5×10^5 conidia/ml) was placed on a multiwell glass slide or cover glass (Matsunami Glass),

694 respectively. Cells were incubated in a humid box for 24 h at 24°C in the dark. Observation of
695 penetration hyphae on cucumber cotyledons and cellophane membranes were performed as
696 previously described (*13*). Appressorial cytorrhysis assay was conducted based on a previous
697 procedure (*68*).
698 A confocal laser scanning microscope LSM900 with Airyscan 2 (Carl Zeiss) equipped with a
699 Plan Apochromat 63×/1.4 Oil DIC objective (Carl Zeiss) was used to acquire confocal
700 microscopic images. Excitation/emission wavelengths were 488 nm/490-556 nm for GFP and
701 561 nm/565-630 nm for mCherry. Images were acquired and processed using ZEN Software
702 (Version 3.1; Carl Zeiss) and Imaris (Version 9.3.1; Bitplane). For detection of appressorial
703 actin assembly, cells were observed using a Zeiss Axio Imager M2 Upright microscope (Carl
704 Zeiss) equipped with a Plan Apochromat 100× oil immersion lens, an Axio Cam MRm digital
705 camera and excitation/barrier filter set of 595 nm/620 nm for RFP. Images were acquired using
706 Axiovision 4.8. Bright-field microscopy was performed using a Nikon ECLIPSE E600
707 microscope equipped with a 40× water immersion lens (Nikon) and an OLYMPUS DP74
708 digital camera system.
709
710

711 **Microarray analysis**
712 For sampling appressoria, the abaxial surface of cucumber cotyledons or cellophane
713 membranes (Wako Chemicals) were inoculated with 10 μL droplets or 10 mL, respectively, of
714 a conidial suspension (1×10^6 conidia/ml), and then incubated at 24°C in a humid box. After
715 16 h, the cellophane was frozen in liquid nitrogen. After 24 h, the lower epidermis of the
716 cotyledons was peeled off. All samples were ground in liquid nitrogen, and total RNA was
717 prepared using the Maxwell RSC Plant RNA Kit (Promega) and the Agilent Plant RNA
718 Isolation MiniKit (Agilent Technologies). Microarray analyses were performed as described
719 previously (*13*) using the *C. orbiculare* ($8 \times 60,000$, 13,352 independent probes, Design ID:
720 060762) oligo microarray, according to the Agilent 60-mer Oligo Microarray Processing
721 Protocol (Agilent Technologies). The normalization condition: i) intensity-dependent Lowess
722 normalization; ii) data transformation, measurements less than 0.01 were set to 0.01; iii) per-
723 chip 75th-percentile normalization of each array; and iv) the expression values per gene were
724 median normalized. The normalized data were subjected to a *t* test, with statistically significant
725 gene sets defined as those giving *P* values less than 0.05. The differentially-regulated genes
726 (fold change > 2 and *P*< 0.05) were selected and were used for further analysis. Functional
727 classification was based on the Gene Ontology (GO), protein families (Pfam) and *C. orbiculare*
728 genome information of CAZymes and SSPs. Note that to avoid redundancy in the count of up-
729 and downregulated genes, all sequences considered as CAZymes were not counted in the
730 broader classes of Hydrolases/Transferases/Oxidoreductases.

References and Notes:

1. S. Kamoun, N. J. Talbot, M. Tofazzal Islam, Plant health emergencies demand open science: Tackling a cereal killer on the run. *PLoS Biol.* **17**, 1–6 (2019).

2. M. C. Fisher, N. J. Hawkins, D. Sanglard, S. J. Gurr, Worldwide emergence of resistance to antifungal drugs challenges human health and food security. *Science.* **360**, 739–742 (2018).

3. R. Dean, J. A. L. Van Kan, Z. A. Pretorius, K. E. Hammond-Kosack, A. Di Pietro, P. D. Spanu, J. J. Rudd, M. Dickman, R. Kahmann, J. Ellis, G. D. Foster, The Top 10 fungal pathogens in molecular plant pathology. *Mol. Plant Pathol.* **13**, 414–430 (2012).

4. C. Beimforde, K. Feldberg, S. Nylinder, J. Rikkinen, H. Tuovila, H. Dörfelt, M. Gube, D. J. Jackson, J. Reitner, L. J. Seyfullah, A. R. Schmidt, Estimating the Phanerozoic history of the Ascomycota lineages: Combining fossil and molecular data. *Mol. Phylogenet. Evol.* **78**, 386–398 (2014).

5. X. Liang, B. Wang, Q. Dong, L. Li, J. A. Rollins, R. Zhang, G. Sun, Pathogenic adaptations of *Colletotrichum* fungi revealed by genome wide gene family evolutionary analyses. *PLoS One.* **13**, e0196303 (2018).

6. L. S. Ryder, N. J. Talbot, Regulation of appressorium development in pathogenic fungi. *Curr. Opin. Plant Biol.* **26**, 8–13 (2015).

7. J. C. De Jong, B. J. McCormack, N. Smirnoff, N. J. Talbot, Glycerol generates turgor in rice blast. *Nature.* **389**, 244–245 (1997).

8. Y. Kubo, I. Furusawa, in *The Fungal Spore and Disease Initiation in Plants and Animals*, G. T. Cole, H. C. Hoch, Eds. (Springer US, Boston, MA, 1991), pp. 205–218.

9. Z. Chen, M. C. Silva, C. J. Rodriguesjr, Appressorium Turgor Pressure of *Colletotrichum kahawae* Might Have a Role in Coffee Cuticle Penetration. *Mycologia.* **96**, 1199–1208 (2004).

10. L. S. Ryder, Y. F. Dagdas, M. J. Kershaw, C. Venkataraman, A. Madzvamuse, X. Yan, N. Cruz-Mireles, D. M. Soanes, M. Oses-Ruiz, V. Styles, J. Sklenar, F. L. H. Menke, N. J. Talbot, A sensor kinase controls turgor-driven plant infection by the rice blast fungus. *Nature.* **574**, 423–427 (2019).

11. M. He, J. Su, Y. Xu, J. Chen, M. Chern, M. Lei, T. Qi, Z. Wang, L. S. Ryder, B. Tang, M. Osés-Ruiz, K. Zhu, Y. Cao, X. Yan, I. Eisermann, Y. Luo, W. Li, J. Wang, J. Yin, S. M. Lam, G. Peng, X. Sun, X. Zhu, B. Ma, J. Wang, J. Liu, H. Qing, L. Song, L. Wang, Q. Hou, P. Qin, Y. Li, J. Fan, D. Li, Y. Wang, X. Wang, L. Jiang, G. Shui, Y. Xia, G. Gong, F. Huang, W. Wang, X. Wu, P. Li, L. Zhu, S. Li, N. J. Talbot, X. Chen, Discovery of broad-spectrum fungicides that block septin-dependent infection processes of pathogenic fungi. *Nat. Microbiol.* **5**, 1565–1575 (2020).

12. Y. F. Dagdas, K. Yoshino, G. Dagdas, L. S. Ryder, E. Bielska, G. Steinberg, N. J. Talbot, Septin-mediated plant cell invasion by the rice blast fungus, *Magnaporthe oryzae. Science.* **336**, 1590–1595 (2012).

13. S. Kodama, J. Ishizuka, I. Miyashita, T. Ishii, T. Nishiuchi, H. Miyoshi, Y. Kubo, The morphogenesis-related NDR kinase pathway of *Colletotrichum orbiculare* is required for translating plant surface signals into infection-related morphogenesis and pathogenesis. *PLOS Pathog.* **13**, e1006189 (2017).

14. R. O. Rocha, C. Elowsky, N. T. T. Pham, R. A. Wilson, Spermine-mediated tight sealing of the *Magnaporthe oryzae* appressorial pore–rice leaf surface interface. *Nat. Microbiol.* **5**, 1472–1480 (2020).

15. M. C. Giraldo, B. Valent, Filamentous plant pathogen effectors in action. *Nat. Rev. Microbiol.* **11**, 800–814 (2013).

16. A. Djamei, K. Schipper, F. Rabe, A. Ghosh, V. Vincon, J. Kahnt, S. Osorio, T. Tohge, A. R. Fernie, I. Feussner, K. Feussner, P. Meinicke, Y.-D. Stierhof, H. Schwarz, B. Macek, M. Mann, R. Kahmann, Metabolic priming by a secreted fungal effector. *Nature.* **478**, 395–398 (2011).

17. J. A. D. Cooper, W. Smith, M. Bacila, H. Medina, Galactose Oxidase from *Polyporus circinatus*, Fr.*. *J. Biol. Chem.* **234**, 445–448 (1959).

18. P. J. Kersten, T. K. Kirk, Involvement of a new enzyme, glyoxal oxidase, in extracellular H_2O_2 production by *Phanerochaete chrysosporium. J. Bacteriol.* **169**, 2195–2201 (1987).

19. D. (Tyler) Yin, S. Urresti, M. Lafond, E. M. Johnston, F. Derikvand, L. Ciano, J.-G. Berrin, B. Henrissat, P. H. Walton, G. J. Davies, H. Brumer, Structure–function characterization reveals new catalytic diversity in the galactose oxidase and glyoxal oxidase family. *Nat. Commun.* **6**, 10197 (2015).

20. Y. Mathieu, W. A. Offen, S. M. Forget, L. Ciano, A. H. Viborg, E. Blagova, B. Henrissat, P. H. Walton, G. J. Davies, H. Brumer, Discovery of a Fungal Copper Radical Oxidase with High Catalytic Efficiency toward 5-Hydroxymethylfurfural and Benzyl Alcohols for Bioprocessing. *ACS Catal.* **10**, 3042–3058 (2020).

21. S. B. Lee, M. C. Suh, Advances in the understanding of cuticular waxes in *Arabidopsis thaliana* and crop species. *Plant Cell Rep.* **34**, 557–572 (2015).

22. D. Ribeaucourt, B. Bissaro, M. Yemloul, V. Guallar, H. Brumer, F. Lambert, J.-G. Berrin, M. Lafond, Controlled Oxidation of Long-Chain Primary Aliphatic Alcohols by a Fungal Copper-Radical Alcohol Oxidase. *ACS Sustain. Chem. Eng.* **9**, 4411–4421 (2021).

790   23.   K. Parikka, M. Tenkanen, Oxidation of methyl α-D-galactopyranoside by galactose oxidase: products
791   formed and optimization of reaction conditions for production of aldehyde. *Carbohydr. Res.* **344**, 14–20
792   (2009).
793   24.   S. M. Forget, F. R. Xia, J. E. Hein, H. Brumer, Determination of biocatalytic parameters of a copper
794   radical oxidase using real-Time reaction progress monitoring. *Org. Biomol. Chem.* **18**, 2076–2084 (2020).
795   25.   A. Zerva, P. Christakopoulos, E. Topakas, Characterization and application of a novel class II
796   thermophilic peroxidase from *Myceliophthora thermophila* in biosynthesis of polycatechol. *Enzyme*
797   *Microb. Technol.* **75**–**76**, 49–56 (2015).
798   26.   R. J. O'Connell, M. R. Thon, S. Hacquard, S. G. Amyotte, J. Kleemann, M. F. Torres, U. Damm, E. A.
799   Buiate, L. Epstein, N. Alkan, J. Altmüller, L. Alvarado-Balderrama, C. A. Bauser, C. Becker, B. W.
800   Birren, Z. Chen, J. Choi, J. A. Crouch, J. P. Duvick, M. A. Farman, P. Gan, D. Heiman, B. Henrissat, R.
801   J. Howard, M. Kabbage, C. Koch, B. Kracher, Y. Kubo, A. D. Law, M. H. Lebrun, Y. H. Lee, I. Miyara,
802   N. Moore, U. Neumann, K. Nordström, D. G. Panaccione, R. Panstruga, M. Place, R. H. Proctor, D.
803   Prusky, G. Rech, R. Reinhardt, J. A. Rollins, S. Rounsley, C. L. Schardl, D. C. Schwartz, N. Shenoy, K.
804   Shirasu, U. R. Sikhakolli, K. Stüber, S. A. Sukno, J. A. Sweigard, Y. Takano, H. Takahara, F. Trail, H.
805   C. Van Der Does, L. M. Voll, I. Will, S. Young, Q. Zeng, J. Zhang, S. Zhou, M. B. Dickman, P. Schulze-
806   Lefert, E. Ver Loren Van Themaat, L. J. Ma, L. J. Vaillancourt, Lifestyle transitions in plant pathogenic
807   *Colletotrichum* fungi deciphered by genome and transcriptome analyses. *Nat. Genet.* **44**, 1060–1065
808   (2012).
809   27.   P. Gan, K. Ikeda, H. Irieda, M. Narusaka, R. J. O'Connell, Y. Narusaka, Y. Takano, Y. Kubo, K. Shirasu,
810   Comparative genomic and transcriptomic analyses reveal the hemibiotrophic stage shift of *Colletotrichum*
811   fungi. *New Phytol.* **197**, 1236–1249 (2013).
812   28.   Y. Dong, Y. Li, M. Zhao, M. Jing, X. Liu, M. Liu, X. Guo, X. Zhang, Y. Chen, Y. Liu, Y. Liu, W. Ye, H.
813   Zhang, Y. Wang, X. Zheng, P. Wang, Z. Zhang, Global Genome and Transcriptome Analyses of
814   *Magnaporthe oryzae* Epidemic Isolate 98-06 Uncover Novel Effectors and Pathogenicity-Related Genes,
815   Revealing Gene Gain and Lose Dynamics in Genome Evolution. *PLoS Pathog.* **11**, 1–30 (2015).
816   29.   M. Shimizu, Y. Nakano, A. Hirabuchi, K. Yoshino, M. Kobayashi, K. Yamamoto, R. Terauchi, H. Saitoh,
817   RNA-Seq of in planta-expressed *Magnaporthe oryzae* genes identifies MoSVP as a highly expressed gene
818   required for pathogenicity at the initial stage of infection. *Mol. Plant Pathol.* **20**, 1682–1695 (2019).
819   30.   Y. Kubo, Y. Takano, Dynamics of infection-related morphogenesis and pathogenesis in *Colletotrichum*
820   *orbiculare*. *J. Gen. Plant Pathol.* **79**, 233–242 (2013).
821   31.   J. N. Rodriguez-Lopez, A. T. Smith, R. N. F. Thorneley, Role of Arginine 38 in Horseradish Peroxidase.
822   A critical residue for substrate binding and catalysis. *J. Biol. Chem.* **271**, 4023–4030 (1996).
823   32.   B. Bissaro, A. Varnai, Å. K. Røhr, V. G. H. Eijsink, Oxidoreductases and reactive oxygen species in
824   lignocellulose biomass conversion. *Microbiol. Mol. Biol. Rev.* **82** (2018).
825   33.   I. Ayuso-Fernández, F. J. Ruiz-Dueñas, A. T. Martínez, Evolutionary convergence in lignin-degrading
826   enzymes. *Proc. Natl. Acad. Sci. U. S. A.* **115**, 6428–6433 (2018).
827   34.   S. Oide, Y. Tanaka, A. Watanabe, M. Inui, Carbohydrate-binding property of a cell wall integrity and
828   stress response component (WSC) domain of an alcohol oxidase from the rice blast pathogen *Pyricularia*
829   *oryzae*. *Enzyme Microb. Technol.* **125**, 13–20 (2019).
830   35.   D. Kozakov, R. Brenke, S. R. Comeau, S. Vajda, PIPER: An FFT-based protein docking program with
831   pairwise potentials. *Proteins Struct. Funct. Bioinforma.* **65**, 392–406 (2006).
832   36.   R. Evans, M. O'Neill, A. Pritzel, N. Antropova, A. Senior, T. Green, A. Žídek, R. Bates, S. Blackwell, J.
833   Yim, O. Ronneberger, S. Bodenstein, M. Zielinski, A. Bridgland, A. Potapenko, A. Cowie, K.
834   Tunyasuvunakool, R. Jain, E. Clancy, P. Kohli, J. Jumper, D. Hassabis, Protein complex prediction with
835   AlphaFold-Multimer. *bioRxiv*. 10.04.463034 (2021). doi:10.1101/2021.10.04.463034.
836   37.   K. W. Borrelli, A. Vitalis, R. Alcantara, V. Guallar, PELE: Protein energy landscape exploration. A novel
837   Monte Carlo based technique. *J. Chem. Theory Comput.* **1**, 1304–1311 (2005).
838   38.   F. Fukada, Y. Kubo, *Colletotrichum orbiculare* Regulates Cell Cycle G1/SProgression via a Two-
839   Component GAP and a GTPase to Establish Plant Infection. *Plant Cell.* **27**, 2530–2544 (2015).
840   39.   K. K. Pennerman, G. Yin, J. W. Bennett, Eight-carbon volatiles: prominent fungal and plant interaction
841   compounds. *J. Exp. Bot.* **73**, 487–497 (2022).
842   40.   M. Haddad Momeni, F. Fredslund, B. Bissaro, O. Raji, T. V. Vuong, S. Meier, T. S. Nielsen, V. Lombard,
843   B. Guigliarelli, F. Biaso, M. Haon, S. Grisel, B. Henrissat, D. H. Welner, E. R. Master, J. G. Berrin, M.
844   Abou Hachem, Discovery of fungal oligosaccharide-oxidising flavo-enzymes with previously unknown
845   substrates, redox-activity profiles and interplay with LPMOs. *Nat. Commun.* **12** (2021).
846   41.   J. M. Sanz-Martín, J. R. Pacheco-Arjona, V. Bello-Rico, W. A. Vargas, M. Monod, J. M. Díaz-Mínguez,
847   M. R. Thon, S. A. Sukno, A highly conserved metalloprotease effector enhances virulence in the maize
848   anthracnose fungus *Colletotrichum graminicola*. *Mol. Plant Pathol.* **17**, 1048–1062 (2016).
849   42.   B. Leuthner, C. Aichinger, E. Oehmen, E. Koopmann, O. Müller, P. Müller, R. Kahmann, M. Bölker, P.

H. Schreier, A H2O2-producing glyoxal oxidase is required for filamentous growth and pathogenicity in *Ustilago maydis*. *Mol. Genet. Genomics*. **272**, 639–650 (2005).

43.   A. K. Chaplin, M. L. C. Petrus, G. Mangiameli, M. A. Hough, D. A. Svistunenko, P. Nicholls, D. Claessen, E. Vijgenboom, J. A. R. Worrall, GlxA is a new structural member of the radical copper oxidase family and is required for glycan deposition at hyphal tips and morphogenesis of *Streptomyces lividans*. *Biochem. J.* **469**, 433–444 (2015).

44.   T. M. Vandhana, J.-L. Reyre, S. Dangudubiyyam, J.-G. Berrin, B. Bissaro, J. Madhuprakash, On the expansion of biological functions of Lytic Polysaccharides Monooxygenases. *New Phytol.* **233**, 2380–2396 (2022).

45.   F. Sabbadin, S. Urresti, B. Henrissat, A. O. Avrova, L. R. J. Welsh, P. J. Lindley, M. Csukai, J. N. Squires, P. H. Walton, G. J. Davies, N. C. Bruce, S. C. Whisson, S. J. McQueen-Mason, Secreted pectin monooxygenases drive plant infection by pathogenic oomycetes. *Science*. **373**, 774–779 (2021).

46.   M. Pickl, M. Fuchs, S. M. Glueck, K. Faber, The substrate tolerance of alcohol oxidases. *Appl. Microbiol. Biotechnol.* **99**, 6617–6642 (2015).

47.   E. Morin, S. Miyauchi, H. San Clemente, E. C. H. Chen, A. Pelin, I. de la Providencia, S. Ndikumana, D. Beaudet, M. Hainaut, E. Drula, A. Kuo, N. Tang, S. Roy, J. Viala, B. Henrissat, I. V. Grigoriev, N. Corradi, C. Roux, F. M. Martin, Comparative genomics of *Rhizophagus irregularis*, *R. cerebriforme*, *R. diaphanus* and *Gigaspora rosea* highlights specific genetic features in Glomeromycotina. *New Phytol.* **222**, 1584–1598 (2019).

48.   A. R. Wattam, D. Abraham, O. Dalay, T. L. Disz, T. Driscoll, J. L. Gabbard, J. J. Gillespie, R. Gough, D. Hix, R. Kenyon, D. Machi, C. Mao, E. K. Nordberg, R. Olson, R. Overbeek, G. D. Pusch, M. Shukla, J. Schulman, R. L. Stevens, D. E. Sullivan, V. Vonstein, A. Warren, R. Will, M. J. C. Wilson, H. S. Yoo, C. Zhang, Y. Zhang, B. W. Sobral, PATRIC, the bacterial bioinformatics database and analysis resource. *Nucleic Acids Res.* **42**, D581–D591 (2014).

49.   K. Katoh, D. M. Standley, MAFFT Multiple Sequence Alignment Software Version 7: Improvements in Performance and Usability. *Mol. Biol. Evol.* **30**, 772–780 (2013).

50.   J. Castresana, Selection of Conserved Blocks from Multiple Alignments for Their Use in Phylogenetic Analysis. *Mol. Biol. Evol.* **17**, 540–552 (2000).

51.   A. Stamatakis, RAxML version 8: a tool for phylogenetic analysis and post-analysis of large phylogenies. *Bioinformatics*. **30**, 1312–1313 (2014).

52.   M. Zámocký, Š. Janeček, C. Obinger, Fungal Hybrid B heme peroxidases – unique fusions of a heme peroxidase domain with a carbohydrate-binding domain. *Sci. Rep.* **7**, 9393 (2017).

53.   K. Katoh, J. Rozewicki, K. D. Yamada, MAFFT online service: Multiple sequence alignment, interactive sequence choice and visualization. *Brief. Bioinform.* **20**, 1160–1166 (2018).

54.   I. Letunic, P. Bork, Interactive Tree of Life (iTOL) v4: Recent updates and new developments. *Nucleic Acids Res.* **47**, 256–259 (2019).

55.   J. Jumper, R. Evans, A. Pritzel, T. Green, M. Figurnov, O. Ronneberger, K. Tunyasuvunakool, R. Bates, A. Žídek, A. Potapenko, A. Bridgland, C. Meyer, S. A. A. Kohl, A. J. Ballard, A. Cowie, B. Romera-Paredes, S. Nikolov, R. Jain, J. Adler, T. Back, S. Petersen, D. Reiman, E. Clancy, M. Zielinski, M. Steinegger, M. Pacholska, T. Berghammer, S. Bodenstein, D. Silver, O. Vinyals, A. W. Senior, K. Kavukcuoglu, P. Kohli, D. Hassabis, Highly accurate protein structure prediction with AlphaFold. *Nature*. **596**, 583–589 (2021).

56.   M. Hebditch, J. Warwicker, Web-based display of protein surface and pH-dependent properties for assessing the developability of biotherapeutics. *Sci. Rep.* **9**, 1–9 (2019).

57.   J. Kyte, R. F.Doolittle, A simple method for displaying the hydropathic character of a protein. *J. Mol. Biol.* **157**, 105–132 (1982).

58.   G. Madhavi Sastry, M. Adzhigirey, T. Day, R. Annabhimoju, W. Sherman, Protein and ligand preparation: Parameters, protocols, and influence on virtual screening enrichments. *J. Comput. Aided. Mol. Des.* **27**, 221–234 (2013).

59.   M. H. M. Olsson, C. R. SØndergaard, M. Rostkowski, J. H. Jensen, PROPKA3: Consistent treatment of internal and surface residues in empirical p K a predictions. *J. Chem. Theory Comput.* **7**, 525–537 (2011).

60.   J. F. Gilabert, D. Lecina, J. Estrada, V. Guallar, Monte Carlo Techniques for Drug Design : The success case of PELE in *Methods and Principles in Medicinal Chemistry* (John Wiley & Sons, Ltd, pp. 87–103 (2018).

61.   N. Metropolis, A. W. Rosenbluth, M. N. Rosenbluth, A. H. Teller, E. Teller, Equation of state calculations by fast computing machines. *J. Chem. Phys.* **21**, 1087–1092 (1953).

62.   R. A. Friesner, J. L. Banks, R. B. Murphy, T. A. Halgren, J. J. Klicic, D. T. Mainz, M. P. Repasky, E. H. Knoll, M. Shelley, J. K. Perry, D. E. Shaw, P. Francis, P. S. Shenkin, Glide: A New Approach for Rapid, Accurate Docking and Scoring. 1. Method and Assessment of Docking Accuracy. *J. Med. Chem.* **47**, 1739–1749 (2004).

910 63. M. Haon, S. Grisel, D. Navarro, A. Gruet, J. G. Berrin, C. Bignon, Recombinant protein production
911   facility for fungal biomass-degrading enzymes using the yeast *Pichia pastoris*. *Front. Microbiol.* **6**, 1–12
912   (2015).

913 64. M. M. Bradford, A rapid and sensitive method for the quantitation of microgram quantities of protein
914   utilizing the principle of protein-dye binding. *Anal. Biochem.* **72**, 248–254 (1976).

915 65. M. J. Martínez, F. J. Ruiz-Dueñas, F. Guillén, Á. T. Martínez, Purification and catalytic properties of two
916   manganese peroxidase isoenzymes from *Pleurotus eryngii*. *Eur. J. Biochem.* **237**, 424–432 (1996).

917 66. S. Stoll, A. Schweiger, EasySpin, a comprehensive software package for spectral simulation and analysis
918   in EPR. *J. Magn. Reson.* **178**, 42–55 (2006).

919 67. R. Ménard, G. Verdier, M. Ors, M. Erhardt, F. Beisson, W. H. Shen, Histone H2B monoubiquitination is
920   involved in the regulation of cutin and wax composition in *Arabidopsis thaliana*. *Plant Cell Physiol.* **55**,
921   455–466 (2014).

922 68. S. Tanaka, K. Yamada, K. Yabumoto, S. Fujii, A. Huser, G. Tsuji, H. Koga, K. Dohi, M. Mori, T.
923   Shiraishi, R. O'Connell, Y. Kubo, *Saccharomyces cerevisiae* SSD1 orthologues are essential for host
924   infection by the ascomycete plant pathogens *Colletotrichum lagenarium* and *Magnaporthe grisea*. *Mol.*
925   *Microbiol.* **64**, 1332–1349 (2007).

926 69. M. Kimura, K. Izawa, K. Yoneyama, T. Arie, T. Kamakura, A Novel Transformation System for
927   *Pyricularia Oryzae*: Adhesion of Regenerating Fungal Protoplasts to Collagen-Coated Dishes. *Biosci.*
928   *Biotechnol. Biochem.* **59**, 1177–1180 (1995).

929 70. N. Ishida, S. Akai, Relation of Temperature to Germination of Conidia and Appressorium Formation in
930   *Colletotrichum lagenarium*. *Mycologia*. **61**, 382–386 (1969).

931 71. K. Saitoh, M. Nishimura, Y. Kubo, N. Hayashi, E. Minami, Y. Nishizawa, Construction of a Binary
932   Vector for Knockout and Expression Analysis of Rice Blast Fungus Genes. *Biosci. Biotechnol. Biochem.*
933   **72**, 1380–1383 (2008).

934 72. A. J. Vanden Wymelenberg, D. Cullen, R. N. Spear, B. Schoenike, J. H. Andrews, Expression of green
935   fluorescent protein in *Aureobasidium pullulans* and quantification of the fungus on leaf surfaces.
936   *Biotechniques*. **23**, 686–690 (1998).

937 73. G. Tsuji, S. Fujii, S. Tsuge, T. Shiraishi, Y. Kubo, *Mol. Plant. Microbe. Interact.*, **16**, 315-325 (2003).

938 74. A. Levasseur, E. Drula, V. Lombard, P. M. Coutinho, B. Henrissat, Expansion of the enzymatic repertoire
939   of the CAZy database to integrate auxiliary redox enzymes. *Biotechnol. Biofuels*. **6**, 41 (2013).

940 75. R. Baroncelli, D. B. Amby, A. Zapparata, S. Sarrocco, G. Vannacci, G. Le Floch, R. J. Harrison, E. Holub,
941   S. A. Sukno, S. Sreenivasaprasad, M. R. Thon, Gene family expansions and contractions are associated
942   with host range in plant pathogens of the genus *Colletotrichum*. *BMC Genomics*. **17**, 1–17 (2016).

943 76. T. Choinowski, W. Blodig, K. H. Winterhalter, K. Piontek, The crystal structure of lignin peroxidase at
944   1.70 Å resolution reveals a hydroxy group on the C(β) of tryptophan 171: A novel radical site formed
945   during the redox cycle. *J. Mol. Biol.* **286**, 809–827 (1999).

946 77. M. Sundaramoorthy, K. Kishi, M. H. Gold, T. L. Poulos, Preliminary Crystallographic Analysis of
947   Manganese Peroxidase from *Phanerochaete chrysosporium*. *J. Mol. Biol.* **238**, 845–848 (1994).

948 78. M. Pérez-Boada, F. J. Ruiz-Dueñas, R. Pogni, R. Basosi, T. Choinowski, M. J. Martínez, K. Piontek, A.
949   T. Martínez, Versatile peroxidase oxidation of high redox potential aromatic compounds: Site-directed
950   mutagenesis, spectroscopic and crystallographic investigation of three long-range electron transfer
951   pathways. *J. Mol. Biol.* **354**, 385–402 (2005).

952 79. N. Ito, S. E. V Phillips, C. Stevens, Z. B. Ogel, M. J. McPherson, J. N. Keen, K. D. S. Yadav, P. F.
953   Knowles, Novel thioether bond revealed by a 1.7 Å crystal structure of galactose oxidase. *Nature*. **350**,
954   87–90 (1991).

955 80. C. L. L. Pham, A. Rey, V. Lo, M. Soulès, Q. Ren, G. Meisl, T. P. J. Knowles, A. H. Kwan, M. Sunde,
956   Self-assembly of MPG1, a hydrophobin protein from the rice blast fungus that forms functional amyloid
957   coatings, occurs by a surface-driven mechanism. *Sci. Rep.* **6**, 25288 (2016).

958 81. N. Ishida, S. Akai, Relation of Temperature to Germination of Conidia and Appressorium Formation in
959   *Colletotrichum lagenarium*. *Mycologia*. **61**, 382–386 (1969).

960 82. J. Sperschneider, P. N. Dodds, EffectorP 3.0: Prediction of Apoplastic and Cytoplasmic Effectors in Fungi
961   and Oomycetes. *Mol. Plant. Microbe. Interact.* **35**, 146–156 (2022).

962 83. G. Vaaje-Kolstad, Z. Forsberg, J. S. Loose, B. Bissaro, V. G. Eijsink, Structural diversity of lytic
963   polysaccharide monooxygenases. *Curr. Opin. Struct. Biol.* **44**, 67–76 (2017).

Supplementary Materials:
Figures S1-S11
Tables S1-S6
Movies S1